Three-body correlations and conditional forces in suspensions of active hard disks

Andreas Härtel,[1,*] David Richard,[2] and Thomas Speck[2]

[1]*Institute of Physics, University of Freiburg, Hermann-Herder-Straße 3, 79104 Freiburg, Germany*

[2]*Institute of Physics, Johannes Gutenberg-University Mainz, Staudinger Weg 9, 55128 Mainz, Germany*

(Received 3 August 2017; revised manuscript received 7 November 2017; published 11 January 2018)

Self-propelled Brownian particles show rich out-of-equilibrium physics, for instance, the motility-induced phase separation (MIPS). While decades of studying the structure of liquids have established a deep understanding of passive systems, not much is known about correlations in active suspensions. In this work we derive an approximate analytic theory for three-body correlations and forces in systems of active Brownian disks starting from the many-body Smoluchowski equation. We use our theory to predict the conditional forces that act on a tagged particle and their dependence on the propulsion speed of self-propelled disks. We identify preferred directions of these forces in relation to the direction of propulsion and the positions of the surrounding particles. We further relate our theory to the effective swimming speed of the active disks, which is relevant for the physics of MIPS. To test and validate our theory, we additionally run particle-resolved computer simulations, for which we explicitly calculate the three-body forces. In this context, we discuss the modeling of active Brownian swimmers with nearly hard interaction potentials. We find very good agreement between our simulations and numerical solutions of our theory, especially for the nonequilibrium pair-distribution function. For our analytical results, we carefully discuss their range of validity in the context of the different levels of approximation we applied. This discussion allows us to study the individual contribution of particles to three-body forces and to the emerging structure. Thus, our work sheds light on the collective behavior, provides the basis for further studies of correlations in active suspensions, and makes a step towards an emerging liquid state theory.

DOI: 10.1103/PhysRevE.97.012606

I. INTRODUCTION

Research on active matter recently revealed exciting new phenomena at the intersection of physics, chemistry, and biology [1–13]. It deals with particles and individuals that show self-propelled motion, which includes living "matter" like fish, flocks of birds [14], and bacteria [4,15], as well as artificial colloidal swimmers [6,11,13,16–20] and robots [21]. Accordingly, detailed knowledge of the fundamental mechanisms that drive active systems is important to understand and control swimming mechanisms and self-organization phenomena such as collective motion [7,22], phase separation due to motility differences [9,23], and formation of periodic stripe patterns [4]. The rich variation of nonequilibrium phenomena in active matter results in potential applications in self-assembly and materials research [24].

The fundamental mechanisms in active many-body systems can be studied with methods from out-of-equilibrium statistical physics. Beyond the well-studied behavior of equilibrated passive systems, new concepts are needed in active systems, for instance, to define pressure [25,26]. The motion of active particles is governed by many different driving mechanisms such as amoeboid or human swimming [1,27], running of animals on land [28], phoretic motion [6,17,29], use of flagella [30,31], and rocket propulsion where fuel is expelled. Depending on whether their shapes and pair interactions are apolar or polar [2,7], active particles can also show nematic ordering [2,3,7,15,32,33]. Further, the coupling of active particles to hydrodynamic interactions determines whether systems behave wet or dry, where the theoretical description of dry systems does not include an explicit solvent [7]. For this reason, the identification of model organisms [10] and minimal models [27,34–45] is important to isolate and study basic principles.

One minimal model for active matter is the model of active Brownian particles, which combines volume exclusion and Brownian directed motion but neglects long-range phoretic and hydrodynamic interactions. Accordingly, this model of "scalar active matter" solely involves scalar fields [46]. The model shows many phenomena when self-propelled individuals (swimmers) interact with surfaces, channels, and traps [37,44,45] or with additional passive particles [41,47]. In bulk it describes a motility-induced phase separation (MIPS) [9,20,36,40,48], where repulsive Brownian swimmers separate in dense and dilute phases at sufficiently high propulsion speeds and number densities even in the absence of cohesive forces.

To unveil the fundamental mechanism of MIPS, previous and the present work use the Smoluchowski equation [49] for the time evolution of the distribution of particle positions [40,47,50]. Until now, the set of hierarchically connected equations was closed only on the two-particle level [40,47], which already allows to define an anisotropy parameter ζ_1 that describes the anisotropy of the pair-distribution function around a tagged particle [40]. The parameter ζ_1 is strongly correlated to the propulsion speed of a single particle and presents a key ingredient for the theoretical description of MIPS [40]. To go beyond one-body densities and in order to *a priori* predict

*Corresponding author: andreas.haertel@physik.uni-freiburg.de

two-body correlations, forces, and effective swimming speeds, one has to consider three-body correlations. This is the aim of the present work. Studying them and finding reasonable approximations will allow us to set up an analytical theory that describes conditional three-body forces and their preferred directions for self-propelled Brownian particles. Moreover, it will enable us to define effective hard-disk coefficients that have the potential to act as order parameters for active systems.

Already in passive colloidal systems not much work has explicitly addressed three-body correlations [51,52] and three-body forces actually have not explicitly been reported in this field at all. One reason might be the difficulty of finding an adequate closure on the three-body level [53–57]. One common closure is the superposition approximation by Kirkwood [51,53,58], which shows reasonable structural agreement with simulations [51] even if it is just a first-order expansion of the triplet distribution function [59]. Thus, research beyond the typical study of two-body correlations might give additional insight into correlations and structure even in passive systems.

In the present work we study three-body correlations and forces in suspensions of active Brownian particles using theory and simulations. In Sec. II we develop the general theoretical framework beyond the two-body level based on the Smoluchowski equation for active Brownian particles. In order to find a closed form of our theory, we apply the Kirkwood superposition approximation. We further focus on the special case of completely steric pair interactions (hard disks) to achieve analytical results for averaged three-body forces in active systems. In Sec. III we first present data from Brownian dynamics simulations. Then we compare these data with our analytical results. In addition, we solve our theoretical framework numerically. By comparing our results from these numerical calculations, the analytical theory, and the simulations, we establish the range of validity and identify limitations of our theory. We discuss in Sec. IV our results and theoretical predictions for active systems and summarize in Sec. V.

II. THEORY

In this section we derive step by step an analytical theory for the microscopic structure of active Brownian particles that interact via a pair potential. Intermediate results are valid for general pair interactions and some of these results are even exact. We structure our derivation as follows. First, in Sec. II A we formulate the general model and framework and in Sec. II B we introduce the relevant variables. Then in Sec. II C we take advantage of symmetries to further reduce the number of parameters and in Sec. II D we discuss the closure of the ensuing hierarchy of equations. Only then do we restrict our theory in Sec. II E to the special case of hard disks and simplify in Sec. II F our closure relation from Sec. II D. Finally, in Sec. II G we expand the pair-distribution function to achieve our final analytic results.

A. Active Brownian particles

Active Brownian particles (ABPs) are a minimal model of particles moving in contact with a heat bath and combining directed motion with volume exclusion. Although strictly speaking this model falls into the class of dry active matter without

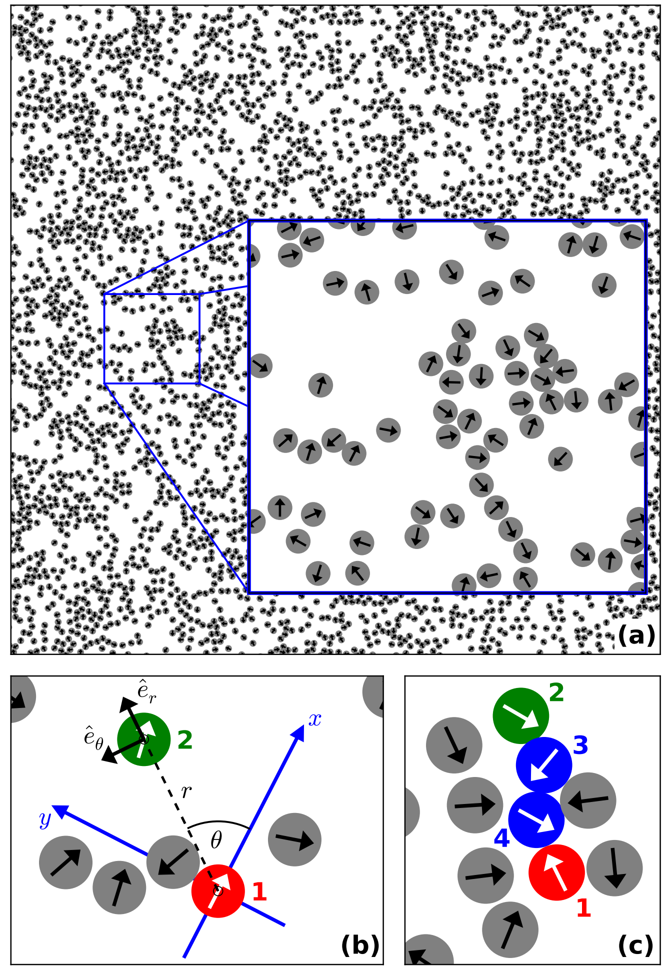

FIG. 1. Simulation snapshot of 4096 self-propelled disks at number density $\bar{\rho} = 0.3$ and constant propulsion speed $v_0/d_{\mathrm{eff}} = 5$. The system size is $L \times L$, with $L \approx 116.85$, and the directions of propulsion $\hat{e}_i$ for each particle i are shown by arrows. (b) Situation from within the snapshot in (a) with two tagged particles and our corresponding relative coordinates. The origin is fixed at the position of the first particle with the x direction along its direction of propulsion. The second particle is located at the position $\vec{r} = (r\cos\theta, r\sin\theta)$. The normalized basis vectors $\hat{e}_r$ and $\hat{e}_\theta$ are shown for the position of particle 2. (c) Situation from within the snapshot in (a) with two tagged particles interacting via two intermediate particles 3 and 4.

an explicit solvent [7], we will use the term "swimming" to describe the directed motion of particles. We consider N particles in a two-dimensional system of area V with mean number density $\bar{\rho} = N/V$, as shown in Fig. 1. The particles at positions $\vec{r}_k$ interact via general radial-symmetric pair potentials $u(r)$ with total potential energy

$$U = \sum_{k<k'} u(|\vec{r}_k - \vec{r}_{k'}|). \tag{1}$$

Every particle is self-propelled, i.e., it swims with a constant propulsion speed v_0 in the direction

$$\hat{e}_k = \begin{pmatrix} \cos(\varphi_k) \\ \sin(\varphi_k) \end{pmatrix}. \tag{2}$$

The coupled equations of motion for the particle positions $\vec{r}_k$ and orientations $\hat{e}_k$ are

$$\dot{\vec{r}}_k = -\mu_0 \vec{\nabla}_k U + v_0 \hat{e}_k + \vec{\xi}_k, \tag{3}$$

$$\dot{\hat{e}}_k = \vec{\eta}_k \times \hat{e}_k, \tag{4}$$

with a mobility μ_0 and the white Gaussian noises $\vec{\xi}_k$ and $\vec{\eta}_k$. We write $\vec{\nabla}_k U(\vec{r}_1,\dots,\vec{r}_N)$ for the partial gradient of the scalar function U, where the gradient is only taken with respect to the k-th parameter $\vec{r}_k$ while all remaining $\vec{r}_i$ with $i \neq k$ are kept fixed. The white Gaussian noises have zero mean and temporal mean-square deviations

$$\langle \vec{\xi}_k(t) \otimes \vec{\xi}_{k'}(t') \rangle = 2D_0 \mathbb{1} \delta_{kk'} \delta(t-t'), \tag{5}$$

$$\langle \vec{\eta}_k(t) \otimes \vec{\eta}_{k'}(t') \rangle = 2D_{\mathrm{r}} \mathbb{1} \delta_{kk'} \delta(t-t'). \tag{6}$$

Here $\mathbb{1}$ denotes the identity matrix. We assume that the spatial diffusion constant D_0 and the rotational diffusion constant D_{r} are hydrodynamically coupled by $D_{\mathrm{r}} = 3D_0/\sigma^2$ [60] such that the no-slip boundary condition holds as in previous work [40,61]; σ is the (effective) particle diameter.

Throughout this work we employ dimensionless quantities and measure lengths in units of σ, time in units of σ^2/D_0, and energy in units of $k_{\mathrm{B}}T$. Here k_{B} denotes Boltzmann's constant and T is the temperature of the system. Consequently, we use $D_{\mathrm{r}} = 3$.

B. Many-body hierarchy

The time evolution of the probability density $P_N(\vec{r}^{\,(N)},\varphi^{(N)};t)$ to find N particles at positions $\vec{r}^{\,(N)}$ with directions of propulsion (orientations) denoted by the angles $\varphi^{(N)}$ is governed by the Smoluchowski equation [49]

$$\partial_t P_N = \sum_{k=1}^{N} \vec{\nabla}_k \cdot [(\vec{\nabla}_k U) - v_0 \hat{e}_k + \vec{\nabla}_k] P_N + D_{\mathrm{r}} \sum_{k=1}^{N} \partial_{\varphi_k}^2 P_N. \tag{7}$$

We use $\vec{r}^{\,(n)}$ as a multi-index denotation for $(\vec{r}_1,\dots,\vec{r}_n)$. The joint probability distribution P_N is normalized to unity, i.e., $\int \cdots \int P_N = 1$. Then we define a hierarchy of n-body densities $\Psi_n \equiv \Psi_n(\vec{r}^{\,(n)},\varphi^{(n)};t)$ for $1 \leqslant n \leqslant N$ by

$$\Psi_n(\vec{r}^{\,(n)},\varphi^{(n)};t) = \int d\vec{r}_{n+1} \cdots d\vec{r}_N \int d\varphi_{n+1} \cdots d\varphi_N \frac{N!}{(N-n)!} P_N. \tag{8}$$

The n-body number densities $\rho_n = \int d\varphi^{(n)} \Psi_n$ at a certain time t are achieved by integrating out the orientations. We further define a conditional one-body probability P_1 in order to describe Ψ_3 in terms of Ψ_2, i.e.,

$$\Psi_3(\vec{r}^{\,(3)},\varphi^{(3)};t) = \Psi_2(\vec{r}^{\,(2)},\varphi^{(2)};t) \frac{N-2}{V} \times V P_1(\vec{r}_3,\varphi_3|\vec{r}^{\,(2)},\varphi^{(2)};t). \tag{9}$$

We also define the conditional distribution

$$g_1(\vec{r}_3|\vec{r}^{\,(2)},\varphi^{(2)};t) = V \int_0^{2\pi} d\varphi_3 P_1(\vec{r}_3,\varphi_3|\vec{r}^{\,(2)},\varphi^{(2)};t), \tag{10}$$

which describes the distribution of a (third) particle when two particles 1 and 2 are given with positions $\vec{r}^{\,(2)}$ and orientational angles $\varphi^{(2)}$. Note that in the limit of large N the factor $(N-2)/V \to \bar{\rho}$.

The integration $\int d\vec{r}_3 \cdots d\vec{r}_N \int d\varphi_3 \cdots d\varphi_N (N-1)N$ on both sides of the Smoluchowski equation (7) leads to

$$\partial_t \Psi_2(\vec{r}_1,\varphi_1,\vec{r}_2,\varphi_2;t) = \sum_{k=1,2} \Big(-\vec{\nabla}_k \cdot \{-[\vec{\nabla}_k u(|\vec{r}_1 - \vec{r}_2|)] + \vec{F}_k + v_0 \hat{e}_k - \vec{\nabla}_k\} \times \Psi_2(\vec{r}_1,\varphi_1,\vec{r}_2,\varphi_2;t) + D_{\mathrm{r}} \partial_{\varphi_k}^2 \Psi_2(\vec{r}_1,\varphi_1,\vec{r}_2,\varphi_2;t) \Big), \tag{11}$$

with the conditional forces

$$\vec{F}_k(\vec{r}_1,\varphi_1,\vec{r}_2,\varphi_2;t) = -\bar{\rho} \int d\vec{r}_3 u'(|\vec{r}_k - \vec{r}_3|) \frac{\vec{r}_k - \vec{r}_3}{|\vec{r}_k - \vec{r}_3|} g_1(\vec{r}_3|\vec{r}_1,\varphi_1,\vec{r}_2,\varphi_2;t). \tag{12}$$

These terms describe the summed contribution of all forces $\vec{F}_{i\to k}$ acting from a particle $i \in \{3,\dots,N\}$ on the respective particle $k \in \{1,2\}$ in the presence of the remaining second particle, i.e., $\vec{F}_k = \sum_{i=3}^{N} \vec{F}_{i\to k}$. This is illustrated in Fig. 1(b), where particles 1 and 2 are shown in red and green, respectively. All third particles that contribute to the conditional forces $\vec{F}_k$ are shown in gray. Note that this formalism is not restricted to a specific pair interaction between individual particles; we only assumed rotational symmetry. In the special case of hard interactions most of the contributions of the gray particles in Fig. 1(b) would vanish, because hard pair interactions lead to forces only when particles touch. For example, only one gray particle in Fig. 1(b) would contribute a nonvanishing force. Similarly, only the blue particles with indices 3 and 4 in Fig. 1(c) would contribute to the direct forces $\vec{F}_1$ and $\vec{F}_2$ in this case. Later we will see that particle 1 is influenced by the presence of particle 2 in the situation shown in Fig. 1(c) via both blue particles 3 and 4. A consequence of the rare event of a particle contact in the case of hard disks is that statistical averaging must be performed over a much larger number of snapshots than in the case of softer interactions, at least when aiming at a similar quality of statistics.

C. Symmetries and parametrization

In the following we focus on the homogeneous phase such that the two-body density $\Psi_2(\vec{r}^{\,(2)},\varphi^{(2)};t)$ depends only on the displacement vector $\vec{r}_2 - \vec{r}_1$. Note that this assumption does not rule out the ability of our theory to study phase separations like MIPS, because the theory is still able to describe both phases individually. Further, divergent behavior in a theory for a homogeneous phase may indicate phase instabilities and thus be a signature of other phases. Our theory still holds for any rotationally symmetric pair-interaction potential $u(r)$. Provided the assumption of a homogeneous phase, we change to relative coordinates in the reference frame of a tagged particle, say, particle 1, such that the tagged particle is oriented in the x direction and its position $\vec{r}_1$ becomes the origin of our coordinate system. Accordingly, the set $\{\vec{r}_1,\varphi_1,\vec{r}_2,\varphi_2\}$ of parameters reduces to the relative position and orientation of the second particle with respect to the first one, as sketched in Fig. 1(b). We parametrize the relative position by $\vec{r}=(r\cos\theta,r\sin\theta)$ such that the normalized directions of the circular coordinates r and θ are $\hat{e}_r=(\cos\theta,\sin\theta)$ and $\hat{e}_\theta=(-\sin\theta,\cos\theta)$. For completeness, the gradient and divergence operators for a vector $\vec{A}$ and a scalar A in these polar coordinates read

$$\vec{\nabla}\cdot\vec{A}=\frac{1}{r}\frac{\partial}{\partial r}(r\hat{e}_r\cdot\vec{A})+\frac{1}{r}\frac{\partial}{\partial\theta}(\hat{e}_\theta\cdot\vec{A}), \tag{13}$$

$$\vec{\nabla}A=\frac{\partial A}{\partial r}\hat{e}_r+\frac{1}{r}\frac{\partial A}{\partial\theta}\hat{e}_\theta. \tag{14}$$

We further transform the two-body density from Eq. (11) into the form of a pair-distribution function by integrating out the orientation φ_2 of the second particle and multiplying by a factor $2\pi/\bar{\rho}^2$, where again we use $(N-1)/V\to\bar{\rho}$ for large N. Accordingly, we obtain

$$\frac{2\pi}{\bar{\rho}}\frac{V}{N-1}\int_0^{2\pi}d\varphi_2\Psi_2(\vec{r}_1,\varphi_1,\vec{r}_2,\varphi_2;t) \xrightarrow[\varphi_1=0]{\vec{r}_2-\vec{r}_1=\vec{r}} g(r,\theta;t) \tag{15}$$

and the Smoluchowski equation (11) becomes

$$\begin{aligned}\partial_t g(r,\theta;t)=\vec{\nabla}\cdot\{&-2[\vec{\nabla}u(r)]+\vec{F}_1(r,\theta;t)-\vec{F}_2(r,\theta;t)\\&+v_0\hat{e}_1+2\vec{\nabla}\}g(r,\theta;t)+D_\mathrm{r}\partial_\theta^2 g(r,\theta;t)\end{aligned} \tag{16}$$

for the pair-distribution function $g(r,\theta;t)$. Consequently, the conditional forces from Eq. (12) now read

$$\vec{F}_1(\vec{r};t)=-\bar{\rho}\int d\varphi_2\int d\vec{r}\,'u'(|\vec{r}\,'|)\frac{-\vec{r}\,'}{|\vec{r}\,'|}g_1(\vec{r}\,'|\,0,0,\vec{r},\varphi_2;t), \tag{17}$$

$$\vec{F}_2(\vec{r};t)=-\bar{\rho}\int d\varphi_2\int d\vec{r}\,'u'(|\vec{r}\,'|)\frac{-\vec{r}\,'}{|\vec{r}\,'|}g_1(\vec{r}\,'|-\vec{r},0,0,\varphi_2;t). \tag{18}$$

D. Closure on the two-body level

In order to obtain a closed form of Eq. (16), we have to determine the conditional distribution $g_1(\vec{r}_3|\cdots)$ that enters the force terms from Eqs. (17) and (18). For this purpose, we apply the Kirkwood superposition approximation [51,53,58], which is attained by the first order of a diagrammatic expansion of the triplet distribution function [59], i.e.,

$$g_{123}=g_{12}g_{13}g_{23}\left[1+\int d\vec{r}_4\int d\varphi_4 f_{14}f_{24}f_{34}+\cdots\right], \tag{19}$$

with f_{ij} the Mayer function and subscripts indicating particle indices [49]. The expansion describes the three-body distribution g_{123} as the sum of products of pairwise distributions between (i) the three particles 1, 2, and 3, (ii) the three particles and one additional fourth particle, (iii) five particles, and so on. The Kirkwood approximation has mainly been applied to systems in equilibrium, but there is no restriction apart from assuming pairwise particle interactions as we have introduced in Eq. (1). By applying the Kirkwood approximation $g_{123}=g_{12}g_{13}g_{23}$ as a closure for our theoretical framework, we find

$$\begin{aligned}&\Psi_3(\vec{r}_1,\varphi_1,\vec{r}_2,\varphi_2,\vec{r}_3,\varphi_3;t)\\&\quad=\Psi_2(\vec{r}_1,\varphi_1,\vec{r}_2,\varphi_2;t)\\&\qquad\times g_2(\vec{r}_2,\varphi_2,\vec{r}_3,\varphi_3;t)g_2(\vec{r}_3,\varphi_3,\vec{r}_1,\varphi_1;t)\Psi_1(\vec{r}_3,\varphi_3;t).\end{aligned} \tag{20}$$

Note that normalization is not contained within the Kirkwood approximation and that the equality in Eq. (20) only holds in the limit of large particle numbers, where $N(N-2)/(N-1)^2\approx 1$. However, our calculations are still valid for any kind of pair interaction $u(r)$. According to Eq. (20), we find closed terms for the conditional distributions that occur in the force terms from Eqs. (17) and (18), i.e.,

$$\begin{aligned}&\int d\varphi_2 g_1(\vec{r}\,'|0,0,\vec{r},\varphi_2;t)\\&\quad=\langle g(|\vec{r}\,'-\vec{r}\,|,\varphi_2;t)\rangle_{\varphi_2}g(|\vec{r}\,'|,\sphericalangle(\vec{r}\,');t),\end{aligned} \tag{21}$$

$$\begin{aligned}&\int d\varphi_2 g_1(\vec{r}\,'|-\vec{r},0,0,\varphi_2;t)\\&\quad=\langle g(|\vec{r}\,'|,\varphi_2;t)\rangle_{\varphi_2}g(|\vec{r}\,'+\vec{r}\,|,\sphericalangle(\vec{r}\,'+\vec{r});t),\end{aligned} \tag{22}$$

where $\langle g(r,\varphi_2;t)\rangle_{\varphi_2}=(2\pi)^{-1}\int_0^{2\pi}d\varphi_2 g(r,\varphi_2;t)$ is an average over angles φ_2 holding the separation fixed and $\sphericalangle(\vec{r}\,)$ denotes the angle enclosed by $\hat{e}_x$ and $\vec{r}$.

E. Special case of hard disks

An important pair interaction is that of hard disks with only steric contributions. The reason is that short-range repulsive potentials can be mapped onto effective hard potentials with an effective particle diameter [62]. Thus, fundamental properties of systems dominantly governed by volume exclusion and packing can be studied and described by one unique model system of hard-core particles.

In the special case of hard disks with diameter σ (1 in our dimensionless units), the pair-interaction potential reads

$$u(r)=\begin{cases}\infty, & r<1\\ 0, & r>1.\end{cases} \tag{23}$$

In this case, the derivative of the pair potential simply becomes $u'(r)=-\delta(r-1)$, where δ denotes the Dirac-δ distribution. Accordingly, the force terms from Eqs. (17) and (18) together with the Kirkwood closure from Eqs. (21) and (22) lead to

$$\begin{aligned}\vec{F}_1(r,\theta;t)=&-\bar{\rho}\int_0^{2\pi}d\theta'\hat{e}(\theta')g(1,\theta';t)\\&\times\langle g(|\hat{e}(\theta')-r\hat{e}(\theta)|,\varphi_2;t)\rangle_{\varphi_2},\end{aligned} \tag{24}$$

$$\begin{aligned}\vec{F}_2(r,\theta;t)=&-\bar{\rho}\int_0^{2\pi}d\theta'\hat{e}(\theta')\langle g(1,\varphi_2;t)\rangle_{\varphi_2}\\&\times g(|\hat{e}(\theta')+r\hat{e}(\theta)|,\sphericalangle[\hat{e}(\theta')+r\hat{e}(\theta)];t),\end{aligned} \tag{25}$$

where $\hat{e}(\theta)=(\cos\theta,\sin\theta)$ denotes a unit vector in the direction of θ. We further rewrite Eq. (16) by using the definition of the operators from Eqs. (13) and (14) and by the pair potential from Eq. (23). Consequently, we find

$$\begin{aligned}\partial_t g(r,\theta;t) = {} & \frac{1}{r}\frac{\partial}{\partial r}\bigg(r\hat{e}_r\cdot\vec{F}_1(r,\theta;t) - r\hat{e}_r\cdot\vec{F}_2(r,\theta;t)\\ & + r v_0\hat{e}_r\cdot\hat{e}_1 + 2r\frac{\partial}{\partial r}\bigg)g(r,\theta;t)\\ & + \frac{1}{r}\frac{\partial}{\partial\theta}\bigg(\hat{e}_\theta\cdot\vec{F}_1(r,\theta;t) - \hat{e}_\theta\cdot\vec{F}_2(r,\theta;t)\\ & + v_0\hat{e}_\theta\cdot\hat{e}_1 + \frac{2}{r}\frac{\partial}{\partial\theta}\bigg)g(r,\theta;t)\\ & + D_{\mathrm{r}}\frac{\partial^2 g(r,\theta;t)}{\partial\theta^2}\end{aligned} \tag{26}$$

for $r > 1$. Since hard disks are not allowed to overlap, the flux in the radial direction at particle-particle contact must vanish with the no-flux condition

$$\begin{aligned}&[\hat{e}_r\cdot\vec{F}_1(r,\theta;t) - \hat{e}_r\cdot\vec{F}_2(r,\theta;t) + \hat{e}_r\cdot\hat{e}_1 v_0]g(r,\theta;t)|_{r=1}\\ &\quad = -2\frac{\partial g(r,\theta;t)}{\partial r}\bigg|_{r=1}.\end{aligned} \tag{27}$$

F. Simplified closure for hard disks

In order to achieve an analytical result, we will further simplify the conditional forces that we derived in the preceding section. It is known that fixing a single particle in bulk leads to a structured radial pair-distribution function. Now fixing a second particle at relative position $\vec{r}$ to the first particle (see Fig. 2) has a twofold outcome: On the one hand, it leads to a direct distribution around the two particles while, on the other hand, an indirect structure develops on top of the direct distribution due to the mutual influence of both fixed particles. For instance, these structures are discussed in a work on three-body correlations in passive systems [51].

These two contributions can also been understood from analyzing the force terms in Eqs. (24) and (25), where two pair-distribution functions cause them, respectively. One contribution stems from the interplay between the third and the fixed particle, on which the respective force $\vec{F}_i$ is acting, while the second contribution arises from the interplay between the third and the remaining second particle. This situation is sketched in Fig. 2(a) for the fixed particle having the index $i = 1$.

To give an example, we first discuss a similar situation where two hard disks are in contact with a third one. This system has been studied by Attard, who proposed an adjusted Kirkwood approximation as a reasonably good closure [63]. The system he studied corresponds to the situation shown in Fig. 2 for $|\vec{r}\,| = 1$, when the second and third particles both are in contact with the particle labeled by 1. The third particle can move along the surface of particle 1 and its position can be parametrized by the enclosed angle θ_Δ. The closure Attard proposed reads [63]

$$g_1(1,1,\cos\theta_\Delta) = g(1)g(1)\bigg(1 + \frac{g(s(\theta_\Delta)) - 1}{2}\bigg), \tag{28}$$

$$s(\theta_\Delta) = \begin{cases}1 + 1(\theta_\Delta - \theta^*), & \theta_\Delta \leqslant \pi\\ 1 + 1(2\pi - \theta_\Delta - \theta^*), & \theta_\Delta > \pi,\end{cases} \tag{29}$$

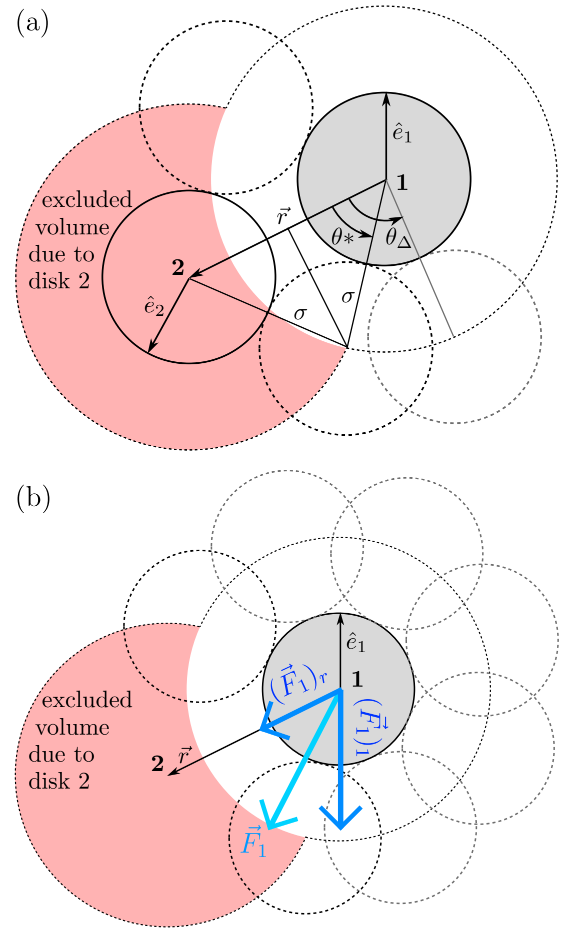

FIG. 2. Sketch for two fixed hard disks labeled 1 and 2 and additional hard disks (dashed) in contact with the first one. The shaded area around particle 2 (red) is not accessible to a third particle due to the presence of the second particle. (a) Angles θ^* and θ_Δ and (b) example of the decomposition of the conditional force $\vec{F}_1$ acting on the first particle. The projected components are $(\vec{F}_1)_r = (\hat{e}_r\cdot\vec{F}_1)\hat{e}_r$ and $(\vec{F}_1)_1 = (\hat{e}_1\cdot\vec{F}_1)\hat{e}_1$.

which is valid for $\theta^* \leqslant \theta_\Delta \leqslant 2\pi - \theta^*$ with $\theta^* = \arccos(1/2) = \pi/3$. For other values of θ_Δ the probability of finding a particle vanishes and $g_1(1,1,\cos\theta_\Delta) = 0$, because particles 2 and 3 are not allowed to overlap. In this approximation, the separation between the two particles 2 and 3 is not measured along a straight line but along the surface of the first particle. The angle $\theta^* = \pi/3$ denotes the limiting case when both particles 2 and 3 are in contact. Note that for separations $r = |\vec{r}\,| > 1$ this angle gets smaller dependent on the separation r.

In our theory, the approximation proposed by Attard [63] relates to the pair-distribution function between particles 2 and 3. This function can be split into two contributions: One simply originates from the excluded volume that the third particle cannot access due to the presence of the second particle; the other contribution stems from the indirect part of the pair distribution between particles 2 and 3. Considering the closure by Attard [63] in Eq. (28), neglecting the second contribution would correspond to approximating the term $(1+\ldots)$ in Eq. (28) as 1. In our theory, we would have to replace the respective pair-distribution function g in the conditional forces in Eqs. (24) and (25) by a spherical step function

$$g(r,\theta) \to \begin{cases} 0, & r < 1 \\ 1, & r \geqslant 1. \end{cases} \tag{30}$$

When we apply this *simplification* to the respective second function g in Eqs. (24) and (25), the conditional forces simplify to

$$\vec{F}_1(r,\theta;t) = -\bar{\rho}\int_0^{2\pi} d\varphi \begin{pmatrix}\cos(\varphi)\\ \sin(\varphi)\end{pmatrix} g(1,\varphi;t) + \bar{\rho}\int_{\theta-\theta^*}^{\theta+\theta^*} d\varphi \begin{pmatrix}\cos(\varphi)\\ \sin(\varphi)\end{pmatrix} g(1,\varphi;t), \tag{31}$$

$$\vec{F}_2(r,\theta;t) = -\bar{\rho}\int_0^{2\pi} d\varphi \begin{pmatrix}\cos(\varphi)\\ \sin(\varphi)\end{pmatrix} \langle g(1,\varphi_2;t)\rangle_{\varphi_2} + \bar{\rho}\int_{\theta+\pi-\theta^*}^{\theta+\pi+\theta^*} d\varphi \begin{pmatrix}\cos(\varphi)\\ \sin(\varphi)\end{pmatrix} \langle g(1,\varphi_2;t)\rangle_{\varphi_2}. \tag{32}$$

The limiting r-dependent angle θ^* that spans the excluded area [see Fig. 2(a)] reads

$$\theta^* = \theta^*(r) = \begin{cases} \arccos(r/2), & 1 \leqslant r \leqslant 2 \\ 0, & r > 2. \end{cases} \tag{33}$$

Now we can identify two main contributions to the conditional forces $\vec{F}_i$ in our theory. We can understand their origin from Fig. 2(b), where an exemplary force $\vec{F}_1$ is constructed from two components. The first component $(\vec{F}_1)_r = (\hat{e}_r \cdot \vec{F}_1)\hat{e}_r$ acts along the separation vector $\vec{r}$. It originates from the excluded volume due to disk 2 such that the surrounding third particles on average push the first particle (approximately) in the direction of the excluded volume. This component is expected to vanish for large separations $r = |\vec{r}\,|$. In our theory, we can see this behavior from Eqs. (31) and (32). If $g(r,\theta;t)$ were homogeneous in the angle θ, the respective second terms on the right-hand sides of Eqs. (31) and (32) would point exactly along the direction of the separation vector $\vec{r}$. The second component $(\vec{F}_1)_1 = (\hat{e}_1 \cdot \vec{F}_1)\hat{e}_1$ along the direction $\hat{e}_1$ of self-propulsion of the first particle clearly originates from collisions with surrounding third particles. This component is expected to be independent of r at large separations and to vanish only in the limit of vanishing propulsion speed v_0. Moreover, the function $g(r,\theta;t)$ is symmetric in the angle θ, i.e., $g(r,\theta;t) = g(r,-\theta;t)$. For this reason, the first term on the right-hand side of Eq. (31) points exactly along the orientation $\hat{e}_1$ of the first particle, while the first term on the right-hand side of Eq. (32) vanishes. In conclusion, the two main directions of the contributions to the conditional forces $\vec{F}_i$, as shown in Fig. 2(b), are the direction of the (normalized) separation vector $\hat{e}_r = \vec{r}/|\vec{r}\,|$ between both tagged particles and the direction of self-propulsion $\hat{e}_1$ of the first particle.

G. Expansion of the pair-distribution function

In this section we derive analytic expressions for the conditional forces, for the effective swimming speed, and for some properties of the pair-distribution function in systems of ABPs. We further define parameters to characterize systems of ABPs following previous work. According to the identification of the two main directions in the preceding section, we will study the projections of the conditional forces onto those directions and derive explicit terms from our theory. In this context, we are solely interested in steady-state solutions of Eq. (26) and for this reason we will skip the parameter t throughout the remaining part of our work.

To achieve analytical expressions for the conditional forces $\vec{F}_i$, we expand the pair-distribution function $g(r,\theta)$ in Fourier modes by

$$g(r,\theta) = \sum_{k=0}^{\infty} g_k(r)\cos(k\theta). \tag{34}$$

We discuss details on the full expansion in the Appendix. When we neglect higher Fourier modes with $k > 1$, we find the resulting projections of the conditional force $\vec{F}_1$ onto $\hat{e}_r$ and $\hat{e}_\theta$ with

$$\hat{e}_r \cdot \vec{F}_1(r,\theta) = 2\bar{\rho} g_0(1)\sin(\theta^*) - \bar{\rho} g_1(1)\left(\pi - \theta^* - \sin(\theta^*)\frac{r}{2}\right)\cos(\theta), \tag{35}$$

$$\hat{e}_\theta \cdot \vec{F}_1(r,\theta) = \bar{\rho} g_1(1)\left(\pi - \theta^* + \sin(\theta^*)\frac{r}{2}\right)\sin(\theta). \tag{36}$$

The limiting angle $\theta^*(r)$ that spans the excluded area due to the presence of particle 2 has been defined in Eq. (33). The angle is shown in Fig. 2 and, for completeness, we give $\sin(\theta^*) = \sqrt{1-(r/2)^2}$. The orientation of the first particle is given by $\hat{e}_1 = \cos(\theta)\hat{e}_r - \sin(\theta)\hat{e}_\theta$ such that we also find

$$\frac{\hat{e}_1 \cdot \vec{F}_1(r,\theta)}{\bar{\rho}} = f_{\mathrm{a}}(r) + f_{\mathrm{b}}(r)\cos(\theta) + f_{\mathrm{c}}(r)\cos(2\theta), \tag{37}$$

$$f_{\mathrm{a}}(r) = g_1(1)[\theta^*(r) - \pi], \tag{38}$$

$$f_{\mathrm{b}}(r) = 2g_0(1)\sin[\theta^*(r)], \tag{39}$$

$$f_{\mathrm{c}}(r) = g_1(1)\sin[\theta^*(r)]\frac{r}{2}. \tag{40}$$

For large separations $r \geqslant 2$ the function θ^* vanishes and we find $\hat{e}_1 \cdot \vec{F}_1(r,\theta) = -\bar{\rho}\pi g_1(1)$. This finding agrees with our expectation from the preceding section, where we discussed that, in this limit, the second particle does not affect the contribution of third particles on the first one anymore. Consequently, we find a constant force along the direction of propulsion of the first particle.

In previous work, Speck *et al.* analyzed the anisotropy of the pair-distribution function for active colloidal disks by studying an anisotropy parameter of this function [40,50,64]. Following the definition of this parameter ζ_1 in previous work [40], we define the first two moments

$$\zeta_0 = -\int_0^\infty dr\, r\, u'(r)\int_0^{2\pi} d\theta\, g(r,\theta), \tag{41}$$

$$\zeta_1 = -\int_0^\infty dr\, r\, u'(r)\int_0^{2\pi} d\theta\, \cos(\theta) g(r,\theta). \tag{42}$$

These parameters can easily be extracted from simulations and could have the role of order parameters in the description of systems of ABPs and their states. For hard disks, we find relations between these parameters and the prefactors $g_i(1)$ in the expansion from Eq. (34) at particle contact ($r = 1$) that read

$$\zeta_0 = 2\pi g_0(1), \tag{43}$$

$$\zeta_i = \pi g_i(1) \quad \forall i \geqslant 1. \tag{44}$$

For almost hard potentials, we will discuss deviations from this equalities in the following sections.

Further insight into our theory is gained by considering the flux $\vec{j}$ that follows from $\partial_t g(r,\theta;t) = -\vec{\nabla} \cdot \vec{j}$ both at particle contact ($r = 1$) and for infinite particle separation ($r \to \infty$). In the case of particle contact, we can combine the expansion (34) and the no-flux condition (27), as shown in the Appendix. In the limit of vanishing propulsion speed $v_0 \to 0$, where all g_k for $k > 0$ vanish, we find $g_0'(1) = -\sqrt{3}g_0(1)g_0(1)\bar{\rho}$ [see Eq. (A9)] as an analytical result for passive systems. In the case of large particle separations $r \to \infty$, both tagged particles are uncorrelated and the flux in the moving reference system is simply given by the effective swimming speed v of the tagged first particle in the opposite direction of propulsion, i.e., $\vec{j} = -v\hat{e}_1$. In this limit, our theory in Eq. (37) predicts a flux $\bar{\rho}\zeta_1\hat{e}_1 - v_0\hat{e}_1$ such that we find the relation

$$v = v_0 - \bar{\rho}\zeta_1 \tag{45}$$

in accord with previous work [40].

III. RESULTS

The first main result of this work is the analytic theory for the microscopic structure around a tagged particle in suspensions of active Brownian particles that we derived in the preceding section. For instance, the theory describes the conditional forces $\vec{F}_k$ as defined in Eq. (12). In order to achieve a more detailed picture and to apply and test our theory, we also perform Brownian dynamics (BD) simulations that we describe in this section first. Then we draw a direct comparison between our theoretical predictions and our results from simulations. In a third step, we test our theory for a general pair-distribution function, i.e., without skipping higher modes in the expansion from Sec. II G. For this purpose, we solve Eq. (26) numerically and compare its solutions to the results from our simulations.

A. Brownian dynamics simulations

We simulate $N = 4096$ two-dimensional Brownian swimmers interacting via the repulsive short-range Weeks-Chandler-Andersen (WCA) potential

$$u_{\mathrm{WCA}}(r) = 4\epsilon\left[\left(\frac{\lambda}{r}\right)^{12} - \left(\frac{\lambda}{r}\right)^{6} + \frac{1}{4}\right] \tag{46}$$

for $r \leqslant r_c = 2^{1/6}\lambda$ and zero otherwise. We employ overdamped dynamics as described in Eq. (3), where $\Delta t = t - t'$ is the time step. The orientation φ undergoes free rotational diffusion with a diffusion constant $D_r = 3D_0/\delta^2$, where δ is the particle diameter. We set δ equal to the effective diameter $\delta = d_{\mathrm{eff}}\lambda$, computed by the Barker-Henderson approximation [62,65]. The energy is scaled by a bath temperature $k_{\mathrm{B}}T$. The repulsive strength ϵ of the potential is set to $100k_{\mathrm{B}}T$, which results in $d_{\mathrm{eff}} = 1.106\,88$. The time step is set to $2 \times 10^{-6}\lambda^2/D_0$.

To obtain the conditional force $\vec{F}_1$ from our BD simulations, we have chosen an equidistant binning of $2\pi/20$ for each angle θ and φ_2, respectively, and $5/500$ for the separation r. To check consistency, we additionally have calculated distribution functions at a higher resolution $2\pi/80$ and $2/1000$; the calculation of distribution functions is less time consuming than the calculation of the three-body forces. We found almost no deviations between the data for both resolutions.

Figure 3 shows data obtained for a number density $\bar{\rho} = 0.3$ and a propulsion speed $v_0/d_{\mathrm{eff}} = 5$. For each of the 80 000 snapshots that we analyzed after the system was equilibrated, we successively tagged two particles and summed up the force contributions of all remaining particles onto the first one. Figures 3(a), 3(d), and 3(g) show the distribution of second particles around the tagged first particle as used for our analysis. The axes correspond to the angular position θ of the second particle in relation to the propulsion direction and position of the tagged first particle, as well as to the orientation angle φ_2 of the second particle relative to that of the first one. This situation is also illustrated in Fig. 1(b). In addition, we sketch a visualization of the different relative positions and orientations in Fig. 3(g) for selected settings. Here the position of the second (red) particle relative to the tagged (black) particle changes along the θ axis and the relative orientation of the second particle (direction of arrows) changes along the φ_2 axis. In the different rows of Fig. 3, we show data for three absolute separations $r \approx 1$ [Figs. 3(a)–3(c)], $r \approx 1.5$ [Figs. 3(d)–3(f)], and $r \approx 4$ [Figs. 3(g)–3(i)]. For small separations of particles 1 and 2 we observe a much higher probability of finding a second particle in front [spot at $(\theta/\pi,\varphi_2/\pi) = (0,1)$ in Fig. 3(a)] than behind [spot at $(1,1)$] the first particle when both particles have opposite orientations. When both particles have the same orientation (when they move together), second particles seem to be distributed uniformly around the first particle [$\varphi_2 = 0$ in Fig. 3(a)]. For increasing separation r between both particles, the observed spots in the distribution get less pronounced [see Fig. 3(d)] and vanish completely in the uniform distribution in Fig. 3(g).

Figures 3(b), 3(e), and 3(h) and Figs. 3(c), 3(f), and 3(i) show the projection of the conditional force $\vec{F}_1$ on the direction of the separation $\vec{r}$ between both tagged particles and on the direction of propulsion of the first particle, respectively. The choice of these directions is motivated by the main directions that can be identified in the conditional forces in Eqs. (31) and (32) and we have discussed their origin and expected values using Fig. 2(b) in Sec. II G. In accordance with these expectations, the value of the projection $\hat{e}_1 \cdot \vec{F}_1$ becomes constant for large separations as shown in Fig. 3(i), because $\vec{F}_1$ becomes parallel to $\hat{e}_1$. Our theory in Sec. II G even predicts the value $\hat{e}_1 \cdot \vec{F}_1 = -\bar{\rho}\zeta_1$, which perfectly fits to a $\zeta_1 \approx 5.0$ that corresponds to the system analyzed in Fig. 3. The uniform distribution further is confirmed by the projection $\hat{e}_r \cdot \vec{F}_1$ in Fig. 3(h), which shows a cosinelike dependence on θ as expected from the definition of $\hat{e}_1 = (1,0)$ and $\hat{e}_r = (\cos\theta, \sin\theta)$ in Sec. II C. At small separations r the excluded-volume effect of the second particle becomes important too. For instance, Fig. 3(c) shows that at $\theta = \pi$ the constant value of approximately -1.6 from Fig. 3(i)

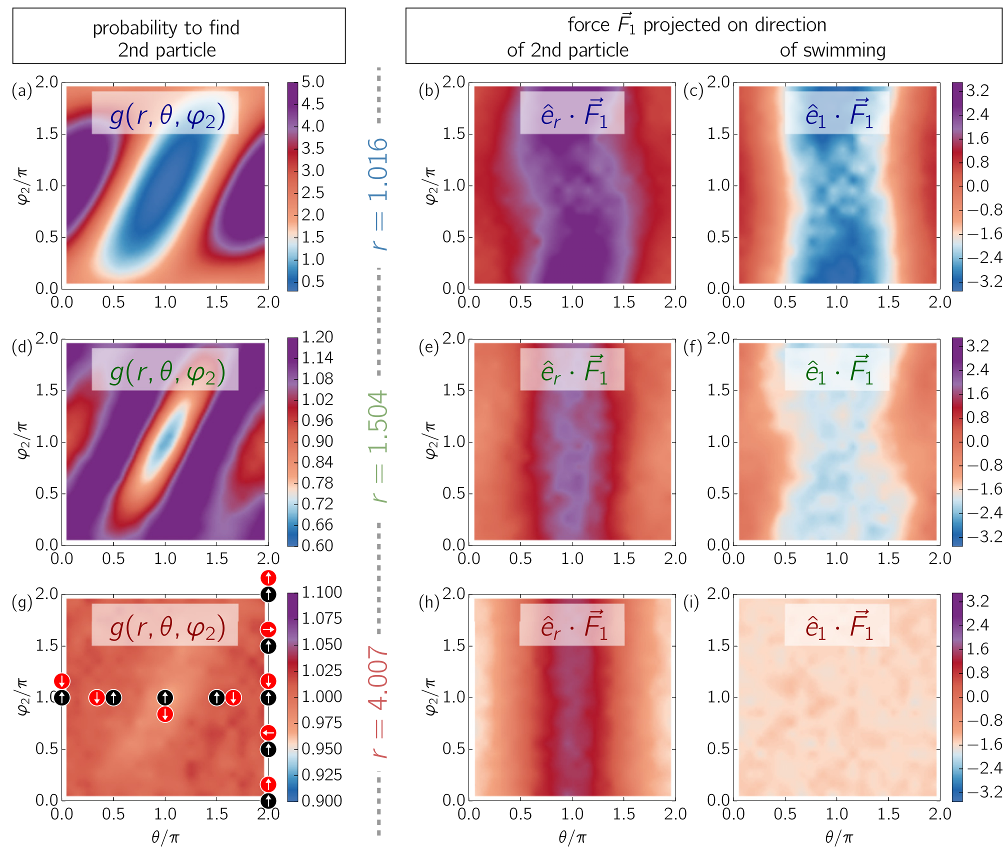

FIG. 3. Pair distribution $g(r,\theta,\varphi_2)$ (first column) and conditional force $\vec{F}_1(r,\theta,\varphi_2)$ (second and third columns) from BD simulations at number density $\bar{\rho} = 0.3$ and propulsion speed $v_0/d_{\text{eff}} = 5$. The first column shows the distribution of a second particle around the first one, the second column shows the projection of $\vec{F}_1$ onto the radial direction $\hat{e}_r$, and the third column shows the projection of $\vec{F}_1$ onto the orientation $\hat{e}_1$. The relative position of the second particle with respect to the first one is given by the separations (a)–(c) $r \approx 1$, (d)–(f) $r \approx 1.5$, and (g)–(i) $r \approx 4$ and by the angle θ, where $\theta = 0$ corresponds to the position in front of the tagged first particle as sketched in Fig. 1(b). The relative orientation of the second particle with respect to the first one is given by φ_2. To help interpret these plots both the relative position θ and the orientation φ_2 are sketched in (g) for certain settings of particles 1 (black) and 2 (red) at the corresponding position in the plot.

has doubled to a value of around -3.2. In this situation, the second particle is located behind the first one such that any third particle likely pushes the first one from ahead due to the excluded volume. This component adds to the collision effect due to the propulsion of the particle. In comparison, at $\theta = 0$ the second particle is located in front of the first one such that the force due to the excluded volume pushes the particle from behind. However, the excluded volume of the second particle in front of the first particle at the same time prevents collisions with third particles such that the absolute value of the projected force in Fig. 3(c) at $\theta = 0$ is only half of the value at $\theta = \pi$.

Moreover, the results in Fig. 3 illustrate that the dependence of the force $\vec{F}_1$ on the orientation φ_2 of the second particle is weak in comparison to the relative position of the second particle. In particular, Figs. 3(c), 3(e), 3(h), and 3(i) show almost no dependence on the orientation φ_2, while Figs. 3(b) and 3(f) show only minor dependences. Interestingly, when particles 1 and 2 are in contact, the dependence on the orientation $\hat{e}_2$ of the second particle is stronger for the projection $\hat{e}_r \cdot \vec{F}_1$ [Fig. 3(b) vs Fig. 3(c)], while at intermediate separations it is stronger for the projection $\hat{e}_1 \cdot \vec{F}_1$ [Fig. 3(f) vs Fig. 3(e)]. Furthermore, we could connect the strength of inhomogeneities in the projection of the force onto $\hat{e}_r$ with the strength of its component due to collisions, if we study the limit of large separations in Figs. 3(h) and 3(i). If this connection would also hold at small separations, the orientation of the second particle would be most important for the force component due to collisions at particle contact ($r \approx 1$) and for the component due to excluded volume at intermediate separations r.

From Fig. 3 we could conclude that the resulting force and its anisotropy are weakened when the separation r between the two particles 1 and 2 is increased. For this reason, we study the dependence of the conditional force $\vec{F}_1$ on the separation r between the two particles in more detail using Fig. 4. To obtain the data shown in Fig. 4 we have averaged over the orientation φ_2 of the second particle, which we previously have seen to have only a minor impact on the force $\vec{F}_1$. The plot in Fig. 4(a) is supported by the three right plots in Figs. 4(b)–4(d) that show data along the marked cutting lines b, c, and d. These supporting plots also present data for additional propulsion speeds. The data clearly show an exception from a monotonic decay of the force strength with increasing separation r at a separation of $r \approx 2$: For a second particle located ahead of the tagged particle, the conditional force shows a strong dip. This dip exists because a third particle exactly fits in between particles 1 and 2 when the second particle is located at $r \gtrsim 2$.

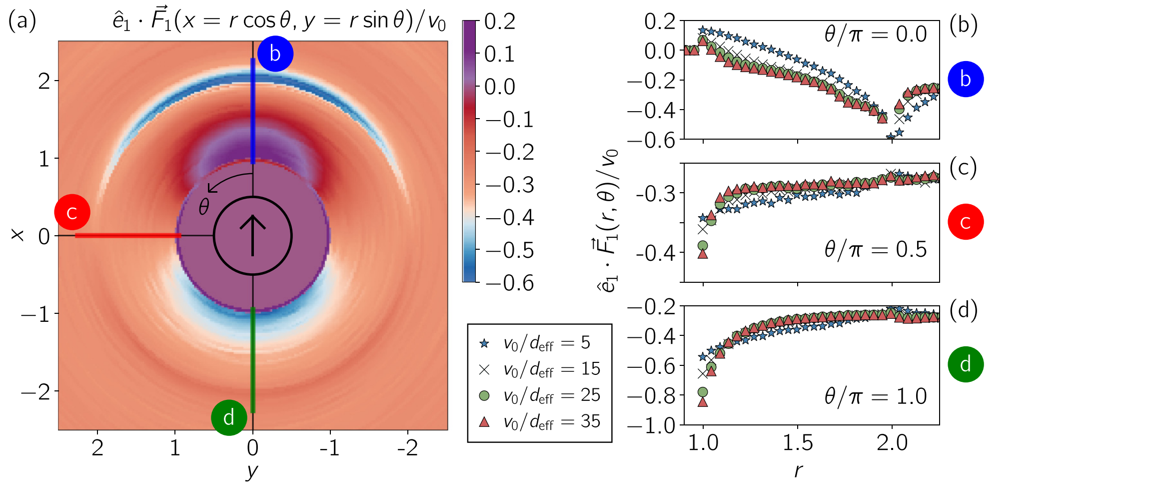

FIG. 4. Projected conditional force $\hat{e}_1 \cdot \vec{F}_1$ on a tagged particle dependent on the relative position (r,θ) of a second particle as obtained from our BD simulations with a number density $\bar{\rho} = 0.3$. Data are shown for (a) propulsion speed $v_0/d_{\rm eff} = 5$ and (b)–(d) speeds 5, 15, 25, and 35. As indicated in (a), the data of (b)–(d) are shown along the cutting lines (b) along the positive x axis (in the direction of propulsion), (c) along the positive y axis (equal to the negative y axis), and (d) along the negative x axis.

This third particle would block the self-propelled particle 1 and create a strong force slowing down the movement of particle 1. A similar but less pronounced reaction would also be expected at around $r \approx 3$ in situations of four particles in a row. Indeed, we have found such settings in our simulations as shown in Fig. 1(c). Note that the dip at $r \gtrsim 2$ and those expected at higher locations are not described by our simplified theory because we have neglected an additional structure between particles 2 and 3 in our assumption from Eq. (30).

We mention that the force term $\vec{F}_1$ overall seems to depend on the propulsion speed linearly, as we see from the collapse of the curves in Figs. 4(b)–4(d). We observe the largest deviations from this linear dependence in the front of the tagged particle [at $\theta = 0$, stars in Fig. 4(b)] and at small propulsion speeds.

B. Test of the theoretical predictions

As a next step, we test our theoretical predictions from Sec. II G by comparing them to our BD simulations. In particular, we are interested in the collapse of data that we have observed in the preceding section in Fig. 4. We follow two routes for our comparison. First, we extract the parameters ζ_i from the pair-distribution functions in our simulations and discuss them in the context of our theory. Second, we compare the theoretical form of the projection $\hat{e}_1 \cdot \vec{F}_1$ in Eq. (37) to the projected force measured in our simulations and shown in Fig. 3. Note that along the second route we also extract the parameters $g_i(1)$ that are contained in the prefactors $f_{\rm a}$, $f_{\rm b}$, and $f_{\rm c}$ of Eq. (37). For hard disks we found the relations from Eqs. (43) and (44) between the ζ_i and the $g_i(1)$.

First, we use Eqs. (41) and (42) to extract the parameters ζ_0 and ζ_1 from our simulation results that we have shown in Fig. 3. We find $\zeta_0 \approx 16.9$ and $\zeta_1 \approx 5.0$. To allow a comparison to our theory, we average the data shown in Fig. 3 over the orientation $\hat{e}_2$ of the second particle, because this parameter has been averaged out in our theory too. The averaged data are presented in Fig. 5. In Fig. 5(a) we show the resulting pair-distribution functions $g(r,\theta)$ from Figs. 3(a), 3(d), and 3(g) together with the predicted function

$$g(1,\theta) = \frac{\zeta_0}{2\pi} + \frac{\zeta_1}{\pi}\cos(\theta) \tag{47}$$

at contact that follows from the extracted ζ_0 and ζ_1 via the first terms of the expansion in Eq. (34). We observe

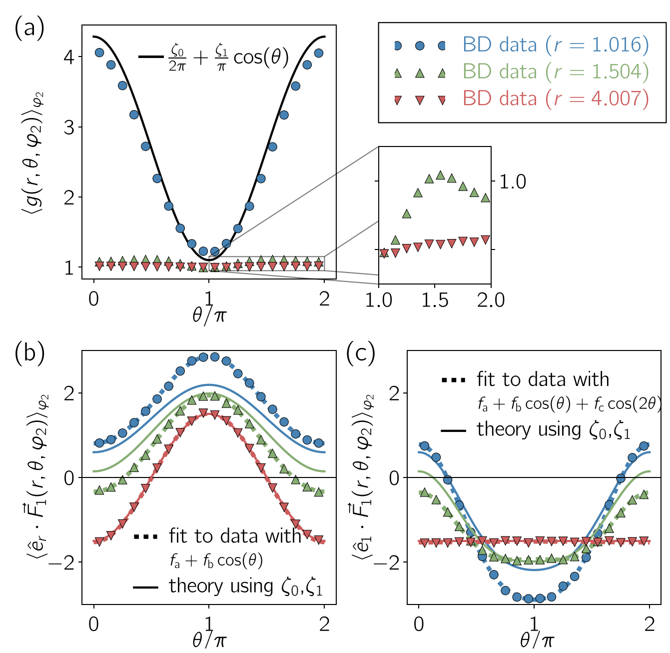

FIG. 5. (a) Pair distribution $\langle g(r,\theta,\varphi_2)\rangle_{\varphi_2}$ and (b) and (c) projected conditional force $\vec{F}_1(r,\theta,\varphi_2)$ as shown in Fig. 3 ($v_0/d_{\rm eff} = 5$ and $\bar{\rho} = 0.3$), but averaged over the angle φ_2 of the relative orientation of the second particle. The plots show the averaged simulation data from Fig. 3 (symbols), least-squares fits to the data in (b) and (c) as noted in the respective legend (dotted lines), and theoretical predictions (solid lines) from (a) Eq. (34), (b) Eq. (35), and (c) Eq. (37). For the theoretical predictions we use the parameters $\zeta_0 = 2\pi g_0(1)$ and $\zeta_1 = \pi g_1(1)$, which we have calculated from our simulations via Eqs. (41) and (42).

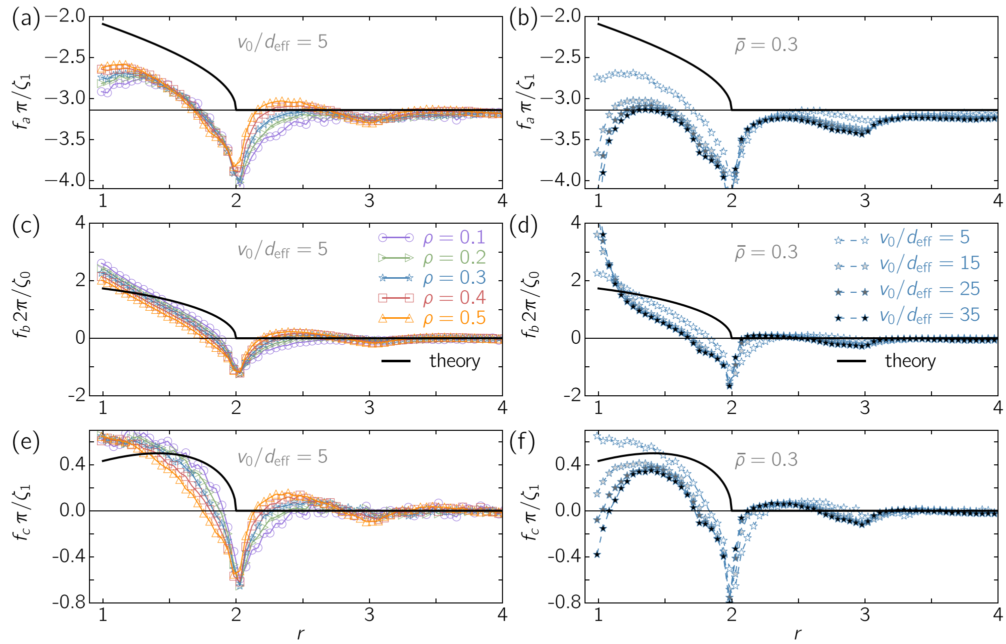

FIG. 6. Coefficients (a) and (b) $f_a\pi/\zeta_1$, (c) and (d) $f_b 2\pi/\zeta_0$, and (e) and (f) $f_c\pi/\zeta_1$ from theory and simulations as defined in Eq. (37). Theoretical curves are given by Eqs. (38)–(40) and simulation results follow from least-squares fits as shown in Fig. 5. Coefficients are shown at (a), (c), and (e) constant propulsion speed v_0 dependent on the number density $\bar\rho$ and (b), (d), and (f) constant number density dependent on the propulsion speed.

minor deviations between the simulation data at $r = 1.016$ and the theoretical prediction using ζ_0 and ζ_1, because the ζ_i correspond to the $g_i(1)$ of hard disks (see also Sec. III C). Overall, the expansion of the pair-distribution function with only two modes captures the simulation data very well at $r \approx 1$ and at large r, but it cannot capture the additional modes that occur at intermediate separations $r \approx 1.5$, which we can see in the inset of Fig. 5(a).

In accord with this finding on the pair-distribution function, we also observe the strongest deviations at intermediate separations $r \approx 1.5$ between the theoretical predictions and simulation data in Figs. 5(b) and 5(c), where we show the φ_2-averaged data of the second and third columns of Fig. 3 together with theoretical results from Eqs. (35) and (37) using $g_0(1) = \frac{\zeta_0}{2\pi}$ and $g_1(1) = \frac{\zeta_1}{\pi}$. In both Figs. 5(b) and 5(c), we additionally show least-squares fits to the simulation data in accord with the respective special form of the theoretical expressions in Eqs. (35) and (37), i.e., $f_a + f_b\cos(\theta)$ in Fig. 5(b) and $f_a + f_b\cos(\theta) + f_c\cos(2\theta)$ in Fig. 5(c). Interestingly, these fits show much better agreement with the simulations than the theoretical predictions based on the ζ_i. This finding might hint at problems in identifying the $g_i(1)$ with the ζ_i, which we did for the theoretical predictions in Fig. 5, although the pair interaction in the simulations is not completely steep. However, the observation confirms the general θ dependence of the projected conditional force just up to the second order. Note that the data shown in Fig. 5(c) are also shown in Fig. 4(a) along spherical cuts around the tagged particle.

According to the previously confirmed θ dependence of the conditional force, now we study the fitting of our simulation data with Eq. (37) in more detail. At the same time, we study the previously mentioned collapse of data onto uniform curves in Figs. 4(b)–4(d). For this purpose, we determine the fitting parameters f_a, f_b, and f_c from least-squares fits of Eq. (37) to the simulation data. We show the resulting parameters for certain combinations of propulsion speed v_0 and density $\bar\rho$ in Fig. 6 and for passive disks with $v_0 = 0$ in Fig. 7. As discussed previously, we replace the parameters $g_i(1)$ within our theory in Eqs. (38)–(40) by the parameters ζ_i via the relations in Eqs. (43) and (44), because the ζ_i are more natural for our simulations of not completely hard disks. The resulting theoretical predictions

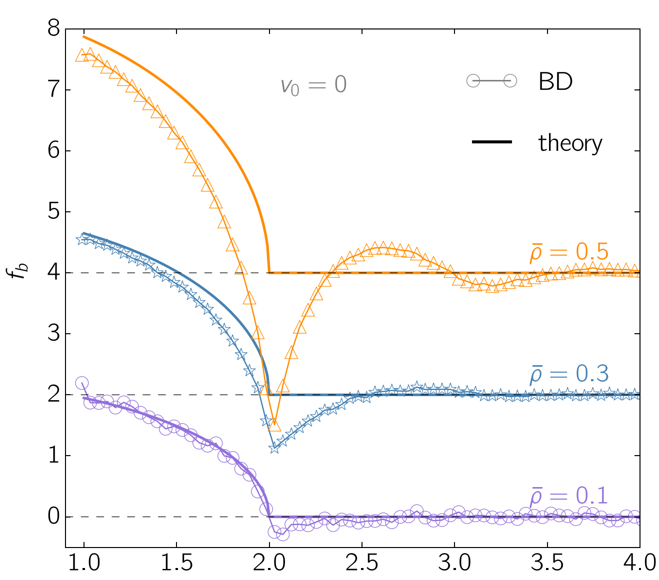

FIG. 7. Coefficient f_b from theory and simulations as defined in Eq. (37) for a system of passive disks. Similar to Fig. 6(c), we show the coefficient f_b dependent on the number density $\bar\rho$. Note that data are shifted to enhance readability. The dashed lines mark zero for each number density $\bar\rho$.

of the coefficients are also shown in Figs. 6 and 7 and they read

$$f_{\mathrm{a}}(r) = \begin{cases} \dfrac{\zeta_1}{\pi}\left[\arccos\left(\dfrac{r}{2}\right) - \pi\right], & r \leqslant 2 \\ -\zeta_1, & r > 2, \end{cases} \tag{48}$$

$$f_{\mathrm{b}}(r) = \begin{cases} \dfrac{\zeta_0}{2\pi}\sqrt{4-r^2}, & r \leqslant 2 \\ 0, & r > 2, \end{cases} \tag{49}$$

$$f_{\mathrm{c}}(r) = \begin{cases} \dfrac{\zeta_1}{\pi}\sqrt{4-r^2}\dfrac{r}{4}, & r \leqslant 2 \\ 0, & r > 2. \end{cases} \tag{50}$$

Note that in Fig. 6 we have removed the linear dependence of the coefficients f_{a} and f_{c} on ζ_1 and of f_{b} on ζ_0 by plotting $f_{\mathrm{a}}(r)\pi/\zeta_1$, $f_{\mathrm{b}}(r)2\pi/\zeta_0$, and $f_{\mathrm{c}}(r)\pi/\zeta_1$. In these cases, our theory in Eqs. (48)–(50) predicts a collapse of the data at different number densities $\bar{\rho}$ and propulsion speeds v_0 to unique and solely r-dependent curves, because the dependences on density and propulsion speed are only contained in the parameters ζ_i.

In accord with this prediction, we find the simulation data in Fig. 6 to be rather independent of the number density in Figs. 6(a), 6(c), and 6(e). However, for different propulsion speeds the data in Figs. 6(b), 6(d), and 6(f) show deviations from a collapse, especially at small propulsion speeds and small separation r. Also in contrast to our theory, the simulation data show detailed radial structure with a pronounced negative peak at $r \approx 2$. This peak matches with our observation of a dip in the data shown in Fig. 4, which we explained by an interaction between the tagged first particle and a second particle via intermediate third particles. The dip is not described in our theory because we closed the Smoluchowski equation using the assumption from Eq. (30) that neglects higher-order structure between the second particle and third particles and we did not consider situations where two particles interact via more than one intermediate particle at all. For instance, we have shown a snapshot from our simulations in Fig. 1(c), where two particles 1 and 2 interact via two additional particles 3 and 4.

We have seen that at large separations r the conditional force $\vec{F}_1$ takes the constant value $-\bar{\rho}\zeta_1\hat{e}_1$. Accordingly, theory and simulation show a value of $-\pi$ (thin line) in Figs. 6(a) and 6(b). This negative value of the coefficient f_{a} describes a θ-averaged effective slow down of the tagged first particle due to third particles, which scales with the propulsion speed v_0 via the parameter ζ_1. The nonuniform shape of the projected force $\hat{e}_1 \cdot \vec{F}_1$ with respect to the location θ of the second particle is captured in the higher-mode coefficients f_{b} and f_{c}. Of course, the relative location of the second particle becomes irrelevant at large r, where both coefficients vanish as shown in Figs. 6(c)–6(f). At $r \approx 1$, the coefficient f_{b} reaches a maximum, which is related to an acceleration of the tagged particle if the second particle is ahead and to a slowdown if it is behind. We argued that the second particle blocks contributions from third particles from the respective direction. Interestingly, we find a change in sign for f_{b} at $r \approx 2$ in Figs. 6(c) and 6(d). Accordingly, the tagged particle now is effectively accelerated by the third particles if the second particle is located behind and it is slowed down if the second particle is ahead. At small separations $r \approx 1$, the simulation data in Fig. 6(b) show a strong deviation from the theoretical prediction that increases with increasing propulsion speed. The simulation shows a much stronger average deceleration of the tagged particle than predicted by the theory. At the same time, we also find a stronger anisotropy in Fig. 6(d) at high propulsion speeds v_0 than predicted by our theory. In this situation of particle contact, third particles are more likely located in simultaneous contact with both tagged particles 1 and 2 than elsewhere, which follows from the Kirkwood closure in Eq. (20) together with the fact that pair distributions of (at least passive) hard disks have maxima at particle contact. Again, this situation is underestimated in our theory due to the assumption from Eq. (30) such that third particles are less likely located in contact with both tagged particles in comparison to simulations. As a result, the tagged particle is predicted to be slowed down less by third particles in our theory if the second particle is located ahead at $(r,\theta) = (1,0)$, which we can observe in Figs. 6(b), 6(d), and 6(f). Note that for the total slowdown of a particle, we have to sum up the contributions from all coefficients. The fact that even Fig. 6(f) shows strong deviations from the theoretical curve might hint at a problem with cutting the expansion of $g(r,\theta)$ after the first mode in Sec. II G.

The deviations between simulations and theory might further hint at problems that arise when the Kirkwood closure is applied to systems of active particles. For a comparison with the active systems, we plot the coefficient f_{b} for passive disks without self-propulsion in Fig. 7. The other coefficients f_{a} and f_{c} vanish for passive disks. Note that, in comparison to Fig. 6, we do not divide f_{b} by ζ_0 and, accordingly, the theoretical curves do not collapse to one unique curve. We furthermore have to use the ζ_0 as an input for our theoretical curves, because we do not independently achieve the parameters from our theory. To improve visibility, we have shifted the data and marked the original zero by horizontal lines, respectively, for each number density. In the limit $r = 1$, we now observe good agreement between theory and simulation for all shown number densities. For increasing density, however, still a dip at $r \approx 2$ develops, but it is less pronounced in comparison to the one observed for self-propelled disks at higher propulsion speed. Of course, deviations between Figs. 7 and 6(d) at $r \approx 1$ could also appear due to the fact that in Fig. 6(d) the coefficient f_{b} is divided by the parameter ζ_0, but such deviations should appear at all values of r, especially at higher ones where the simulation confirms the theory.

In conclusion, we could identify mainly two effects that lead to the observed behavior of the coefficients f_{a}, f_{b}, and f_{c} at the positions $r \approx 1$ and $r \approx 2$, i.e., at particle contact and at the position of the discussed dip. The dip mainly originates from the three-body structure between both tagged particles 1 and 2 and a third particle. It does not appear in our theory, because we neglect the secondary structure beyond volume exclusion between particles 2 and 3 by our approximation from Eq. (30). The behavior at $r \approx 1$ is described well for passive disks within our theory. For self-propelled disks the deviations from the theory originate, next to the missing contribution of structure between particles 2 and 3, from stopping the expansion of $g(r,\theta)$ in Sec. II G at a certain order and from applying the Kirkwood closure in active systems.

C. Pair-distribution function

In our simulations we have full access to the pair-distribution function $g(r,\theta)$ and, using Eqs. (41) and (42), to the parameters ζ_i of its expansion in Eq. (34). In the preceding section we used these parameters from our simulations to test our analytic theory. The theory is derived from the Smoluchowski equation (26), which can also be solved numerically without applying the simplified closure discussed in Sec. II F, which we applied to obtain analytical results. When we use Eq. (26) in order to obtain data for $g(r,\theta)$, the conditional forces $\tilde{F}_i$ that enter Eq. (26) are given in Eqs. (24) and (25) for our system of self-propelled hard disks.

We solve Eq. (26) using a forward-time and center-space scheme [66] on a numerical grid with $(r_i,\theta_{ij}) \in [1,R] \times [0,2\pi]$. For the radial r component we use $N_r = 600$ equidistant grid points and set $R = 6$. For the angular θ component we use equally distributed $N_{\theta,i}$ grid points at each radial index i, respectively, such that the spacing $r_i(\theta_{i,j+1} - \theta_{i,j})$ between two points of indices j and $j+1$ is smaller than or equal to $\Delta_{\text{num}} = 0.1$, i.e., we set $N_{\theta,i} = \lceil 2\pi r_i/\Delta_{\text{num}} \rceil$. Here $\lceil a \rceil$ denotes the rounded up integer of a. Since the number of grid points $N_{\theta,i}$ in the angular direction depends on the radial index i, we use linear interpolation along the angular θ coordinate to perform the center-space scheme in the radial direction. At the boundaries with $r = 1$ and $r = R$, we use Neumann boundary conditions, i.e., we apply the no-flux condition which is given in Eq. (27) for $r = 1$. Outside the grid, we assume $g(r,\theta;t) = 0$ when $r < 1$ and $g(r,\theta;t) = 1$ when $r > R$. As an initial configuration at time t_0, we have chosen $g(r_i,\theta_j;t_0) = 1$ for $r \geqslant 1$. We then run $N_t = 3 \times 10^5$ time steps of size $dt = 10^{-5}$ to achieve a final variation of $\|\partial_t g(r_i,\theta_j;t_{N_t})\| \lesssim 0.02$, where $\|a_{ij}\|$ denotes the maximum norm of a_{ij}. We call this final state the steady-state solution of Eq. (26).

We show our numerical results in comparison to results from our BD simulations in Fig. 8 for three propulsion speeds $v_0 = 0$ [Figs. 8(a)–8(c)], $v_0 = 5$ [Figs. 8(d)–8(f)], and $v_0 = 20$ [Figs. 8(g)–8(i)]. Again, we chose the same density $\bar{\rho} = 0.3$ as studied previously in Fig. 6. The steady-state pair-distribution function $g(r,\theta)$ is symmetric in the angle θ and for this reason we draw half planes only for our BD data (left) and numerical data (right) in Figs. 8(a), 8(d), and 8(g). The plots in these panels are parametrized by $(x,y) = (r\cos\theta, r\sin\theta)$, where the respective length unit is the (effective) particle diameter d_{eff} for the BD data and σ for the numerical data. Furthermore, we show data at particle contact in Figs. 8(b), 8(e), and 8(h), i.e., along the line with $r = 1$ in Figs. 8(a), 8(d), and 8(g), and in

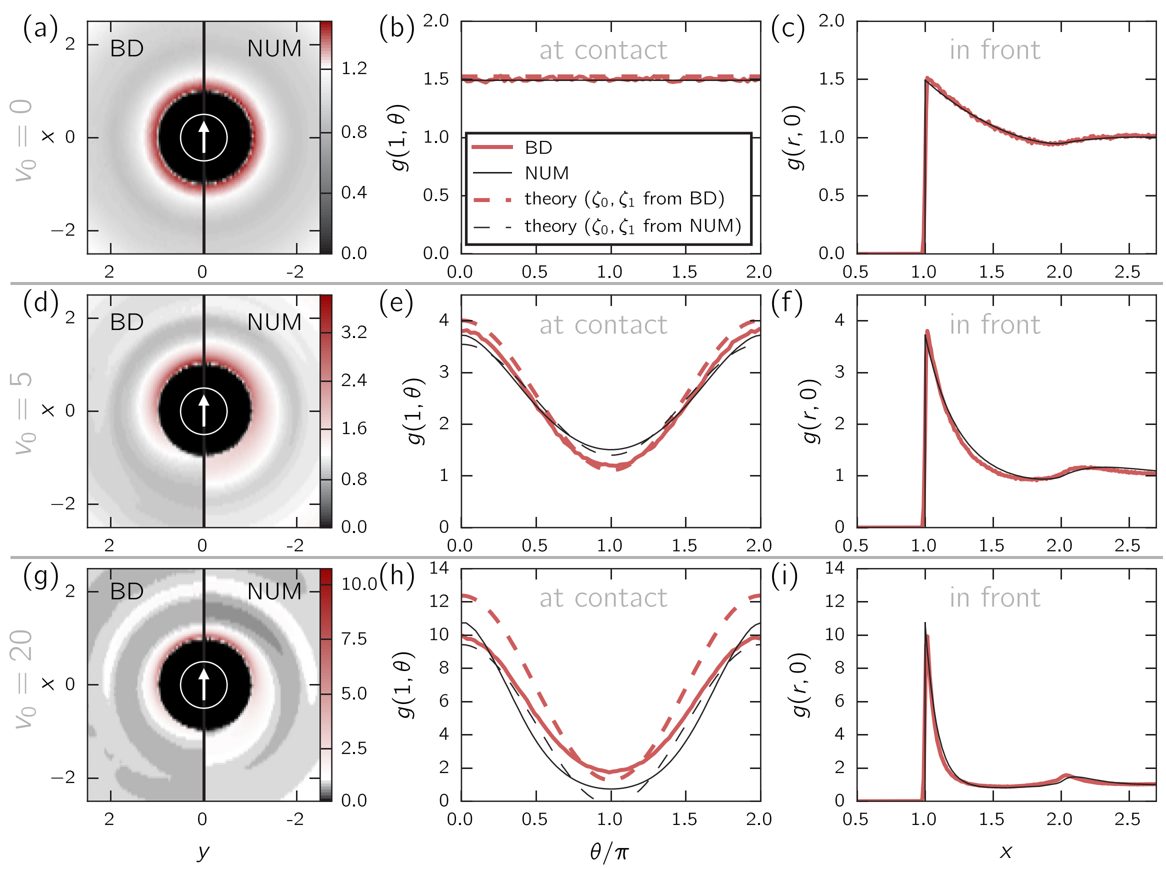

FIG. 8. Pair-distribution functions $g(r,\theta)$ around a self-propelled particle that is located at (0,0) and swims in the positive x direction. We show data at number density $\bar{\rho} = 0.3$ and at propulsion speeds (a)–(c) $v_0 = 0$, (d)–(f) $v_0 = 5$, and (g)–(i) $v_0 = 20$. The full function is shown in (a), (d), and (g) and has the symmetry $g(r,\theta) = g(r,-\theta)$. Accordingly, we show data obtained from our BD simulations (BD) on the left half of the plot and numerical results from our theory (NUM) on the right half of the same plot. (b), (e), and (f) Values at particle contact, where we use the effective diameter as the particle-particle separation in our simulations. In addition, we show the theoretical predictions according to the parameters ζ_0 and ζ_1, which we have calculated from the respective data. Values are presented in Table I. (c), (f), and (i) Function $g(x,0)$ along the positive x axis in front of the tagged particle.

TABLE I. Values for ζ_0 and ζ_1, extracted from our BD simulations and from our numerical solutions of Eq. (26) as shown in Fig. 8. Values are rounded to two digits after the decimal.

$\bar{\rho}$	v_0	ζ_0	ζ_1
		BD simulations	
0.3	0	9.60	
	5	16.08	4.55
	20	42.88	17.46
		Numerical solutions	
0.3	0	9.38	
	5	15.54	3.37
	20	29.08	15.08

front of the particle in Figs. 8(c), 8(f), and 8(i), i.e., along the positive x axis in Figs. 8(a), 8(d), and 8(g). At finite propulsion speed, the data, especially at particle contact, show a peak in the pair-distribution function ahead of the tagged particle and a depletion behind it. While the numerical solutions for $g(r,\theta)$ are overall converged, the exact depth of the minimum at $g(1,\pi)$ in this depletion area is still sensitive with respect to the grid discretization. For the employed grid, the solutions fit well with the results from the numerical simulations. Small deviations between both solutions from theory and simulations are visible for the finite propulsion speeds $v_0 = 5$ and $v_0 = 20$ in Figs. 8(d)–8(i), especially behind the tagged particle.

Having at hand data for the full pair-distribution function $g(r,\theta)$, we can calculate the corresponding parameters ζ_0 and ζ_1 using Eqs. (41) and (42). For our BD and numerical results from Fig. 8 we present these parameters in Table I. We observe that the numerical results from our theory underestimate both the mean-value parameter ζ_0 and the anisotropy parameter ζ_1. The gap between the BD and numerical data increases with increasing propulsion speed v_0. Furthermore, we can use the expansion from Eq. (34) to determine the pair-distribution function $g(r=1,\theta)$ at particle contact from the parameters ζ_0 and ζ_1 via the relations $\zeta_0 = 2\pi g_0(1)$ and $\zeta_1 = \pi g_1(1)$ for hard disks from Eqs. (43) and (44). We show these theoretical curves for parameters ζ_i obtained from the BD and numerical data in Figs. 8(b), 8(e), and 8(f) by dashed lines. While we observe only minor deviations in Figs. 8(b) and 8(e) between the theoretical lines and the corresponding simulation and numerical data, respectively, we find strong deviations in Fig. 8(h). Here the theoretical curve fed by the parameters from BD predicts much higher values in front of the tagged particle than BD itself. Even the average value that is related to ζ_0 is higher than that found in the simulation data. This finding originates from the not completely hard pair potential in Eq. (46) that we used in our simulations, for which the relations between the ζ_i and the $g_i(1)$ do not hold strictly such that the relation becomes inaccurate at high propulsion speed. Indeed, the resulting parameters $g_i(1)$ describe the effective hard pair distribution at contact, which is higher than the smeared-out distribution of the "softer" interaction in our simulations. Of course, the identities hold for hard disks and, accordingly, the theoretical curve fed by the parameters from the numerical data is obeyed on average. However, the predicted values at $\theta = \pi$ behind the tagged particle take slightly negative values, because the shape of the line at particle contact cannot be captured completely by the first two modes of the expansion of the pair-distribution function. The latter shows a very wide minimum for the numerical data in Fig. 8(h) in comparison to the BD data. Apart from the deviations between the numerical and BD results behind the tagged particle, both agree well for the distribution of second particles ahead of the tagged particle, as shown in Figs. 8(c), 8(f), and 8(i). In agreement with our simulations, the numerically obtained pair-distribution function even shows maxima at positions ahead of the self-propelled particle with $r \approx 2$, $r \approx 3$, $r \approx 4$, and so on (only the first is shown in Fig. 8), as we expect from the discussion of the structure of the conditional force $\vec{F}_1$ along with Fig. 4 and in Sec. III B. At high propulsion speeds, these maxima are located slightly farther away from the tagged particle in the numerical results when compared to the BD results, as we find in Fig. 8(c).

IV. DISCUSSION

In the previous sections we have derived an analytical theory for the microscopic structure of active Brownian particles that interact via hard pair potentials. We have analyzed this theory by testing its predictions using BD simulations and by solving the underlying Smoluchowski equation (26) numerically. In this context, we have studied pair-distribution functions and conditional three-body forces between the active particles. In Sec. II F we have identified two main contributions to the averaged conditional force $\vec{F}_1$ that acts on a tagged first particle in the presence of a second tagged particle from all remaining particles. The corresponding two main directions of the conditional force $\vec{F}_1$ are the direction of the (normalized) separation vector $\hat{e}_r = \vec{r}/|\vec{r}\,|$ between both tagged particles and the direction of self-propulsion $\hat{e}_1$ of the first particle. We discussed that these directions originate from the excluded volume due to the presence of the second particle and from the directed motion of the first particle and the resulting collisions with surrounding particles. From another perspective, both directions further correspond to the splitting of the total force that acts on a tagged particle into the conditional force $\vec{F}_1$ and the contribution $\vec{F}_{12}$ from the second particle. In our study we found the dependence of $\vec{F}_{12}$ on the angular position θ at small propulsion speeds of the same order as that of $\vec{F}_1$, but we found the force $\vec{F}_{12}$ and its anisotropy almost independent of the propulsion speed v_0. In contrast, we observed a strong dependence on the propulsion speed for the anisotropy of $\hat{e}_r \cdot \vec{F}_1$. This might lead to situations where, at sufficiently high propulsion speeds, the free energy can be reduced by clustering of particles with a second particle ahead.

Indeed, anisotropic correlations due to the self-propulsion of the particles are a key ingredient for the motility-induced phase separation. However, the system of ABPs still is described solely by the scalar fields number density and propulsion speed. For this reason, the system is still classified as scalar active matter [46], as pointed out in the Introduction.

In our analysis of simulation results in Sec. III A, we found the orientation of the second tagged particle to be rather unimportant. If it is taken into account, the dependence on this orientation is strongest for the collision term of the conditional force $\vec{F}_1$ along the propulsion direction $\hat{e}_1$ at particle-particle contact ($r \approx 1$) and for the excluded-volume term along $\vec{r}$ at intermediate particle separations of $r \approx 1.5$. However, the relative position of the second tagged particle in comparison to the first one is very important, i.e., the angle θ at which the second particle is located around the first one and the separation r. While the anisotropic angular shape of the conditional force $\vec{F}_1$ at a given separation r overall is described well by only two or three modes within our theory at small and large separations, the theory does not describe additional modes that appear at intermediate separations of $r \approx 1.5$. Thus, it might be necessary to also take higher modes into account when intermediate particle separations dominate.

The radial dependence of the conditional force $\vec{F}_1$ on the separation r is most interesting ahead of the tagged first particle in its direction of self-propulsion. In Fig. 4 we have shown that this force has a dip that develops at $r \gtrsim 2$ when the propulsion speed v_0 of the particles is increased. Our theory does not predict this dip, as we have shown in Figs. 6 and 7. As discussed previously, the dip develops at a separation $r \gtrsim 2$ of the first and the second particle, where a third particle fits in between them. This intermediate particle leads to a strong repulsive force between the two tagged particles. The latter is not described by our theory, because we neglect structural correlations between second and third particles beyond volume exclusion for the calculation of the conditional forces $\vec{F}_i$ by applying the approximation in Eq. (30). For example, Fig. 7 shows the coefficient f_b in a system of passive disks that, according to Eqs. (35) and (39), corresponds to the negative strength of the conditional force onto the first particle. When the second particle is located close to the first particle, it blocks third particles from interacting with the first particle in a certain area, as shown in Fig. 2. The amount of surface that is blocked for third particles is described by the angle θ^*. This angle decreases when the separation r increases until the separation between the first and second particles becomes $r \geqslant 2$. Our theory does not assume a higher probability of finding third particles in the vicinity of the second particle due to our assumption made in Eq. (30) such that the conditional force $\vec{F}_1$ vanishes for all $r \geqslant 2$. In the simulations, the probability of finding third particles in the vicinity of the second particle is higher than average and for this reason the simulation data show a pronounced dip around $r = 2$ in Figs. 6 and 7. Note that problems also arise when the assumption from Eq. (30) is used to solve Eq. (26) self-consistently, because the angle θ^* that enters the theory is not continuously differentiable.

Our theory is based on the two-body Smoluchowski equation, which we closed on the three-body level using Kirkwood's approximation. We tested this theoretical framework by calculating its steady-state solutions numerically without applying the assumption from Eq. (30). The numerical solution of our theory does predict the anisotropic structure in the pair-distribution function at moderate propulsion speed that originates from the dip in the conditional forces, as we have shown in Sec. III C and in Fig. 8. At higher propulsion speeds the agreement between our theoretical approach and our simulation results becomes poorer as we observed in Table I for the ζ_i and in Fig. 8. Furthermore, our theoretical approach cannot capture situations where two particles interact via more than one intermediate particle, because the approach is based on a three-body closure. It has been shown that such multiparticle interactions are relevant for active systems [67,68] such that it might be necessary to extend our theory to the four-body level. In our simulations we have observed situations where at least four particles interact, as exemplified in the snapshot in Fig. 1(c).

Our theory in Eqs. (48)–(50) successfully predicts a collapse of the data at different number densities $\bar{\rho}$ and sufficiently high propulsion speeds v_0 onto unique and solely r-dependent curves. The data of all involved coefficients f_a/ζ_1, f_b/ζ_0, and f_c/ζ_1 collapse onto a unique curve, respectively, because the dependences on density and propulsion speed are only contained in the parameters ζ_i. The observed collapse in the simulation data in Figs. 6 and 7 confirms this dependence of the ζ_i on the propulsion speed and the number density and thus indicates the role of the ζ_i as order parameters in systems of ABPs. In Fig. 6 we found the strongest deviations from the collapse to a unique curve at small propulsion speeds and particle separations r. Via a comparison between active and passive disks, we argued that these deviations arise from problems with the applied Kirkwood closure in combination with the activity of the ABPs.

We have seen that our theory predicts the general shape of the anisotropic conditional force and of the two-body distribution function. Its analytic form is based on the expansion of the pair-distribution function in Eq. (34) and on the involved parameters $g_i(r)$. For the hard-disk potential from Eq. (23), we found the equalities in Eqs. (43) and (44) between the contact values $g_i(1)$ of the expansion coefficients and the parameters ζ_i, which are defined in Eqs. (41) and (42). The latter can also be obtained directly from not perfectly hard potentials like the WCA potential in Eq. (46), which we have used in our BD simulations with a very strong coefficient $\epsilon = 100 k_\mathrm{B}T$ to simulate a system of effectively hard disks. Note that for almost hard interactions gradients become steep and the numerical resolution must be chosen appropriately. In Sec. III C we have seen for our simulations of not completely hard disks that the equalities between the parameters ζ_i and values of $g(r)$ at contact do not hold, because contact is not well defined for soft potentials. Indeed, the ζ_i are defined as pair distributions weighted with the derivative of the pair potential and for this reason they represent effective hard-disk coefficients that correspond to the coefficients in the expansion of $g(r)$ at contact for hard disks. In our theory we neglected all higher modes in the expansion in Eq. (34) such that all ζ_i for $i > 1$ vanish. In fact, we have shown that the first two modes ζ_0 and ζ_1 in a system of ABPs already predict the main directions of the acting forces, describe the general anisotropic shape of the conditional forces, and explain the effective swimming speed. The linear relation between the parameter ζ_1 and the propulsion speed v_0 can be seen either from the projection of the conditional force $\hat{e}_1 \cdot \vec{F}_1$, in Figs. 4(b)–4(d), where all data collapse when it is divided by the propulsion speed v_0, or from the fact that the projected conditional force approaches $-\bar{\rho}\zeta_1$ at large separations $r > 2$. This finding further agrees with previous work [40,69], where ζ_1 is discussed to be proportional to v_0 with a proportionality factor of approximately one.

Our analytic theory does not independently predict the parameters ζ_i. However, we have shown that our analytic theory is predictive for given ζ_i and that results are in good agreement with our simulations. We further found that numerical solutions of Eq. (26) together with the conditional forces from Eqs. (24) and (25) agree well with our simulation data.

The corresponding parameters ζ_0 and ζ_1 fit those obtained from our simulations up to moderate propulsion speeds of $v_0 \approx 5$, but we find strong deviations at larger $v_0 \approx 20$. As possible reasons we discussed closing the Smoluchowski equation on the three-body level, the Kirkwood approximation, neglecting additional structure between second and third particles, and stopping the expansion of $g(r)$ after the second-order term. In any case, obtaining the parameters ζ_i from our numerical solutions would make the theory independent such that it could be used to predict MIPS or the pressure in active systems from the combined knowledge of the pair interactions, the free propulsion speed, and the density without any additional input.

V. CONCLUSION

In this work we have studied two-body and especially three-body correlations and conditional forces in systems of active Brownian particles. Based on the many-body Smoluchowski equation, we have developed a theoretical framework that we closed on the three-body level. Applied to the special case of hard-particle interactions, we have derived analytical expressions for conditional three-body forces and identified preferred directions of these forces with respect to the direction of propulsion of tagged particles. We have verified our theory in a detailed comparison with Brownian dynamics computer simulations, for which we have reported three-body forces. In this context we also have discussed discrepancies between the modeling of active particles with hard pair-interaction potentials and soft or almost hard potentials. As a consequence, theoretical models for active systems that are based on hard interaction potentials must be handled carefully when they are applied to systems of not completely hard particles. For future work it might be interesting to also study effective interaction potentials within our theory as performed in recent work [70].

We further have identified the range of validity and limitations of our theory. While we have found generally good agreement between theory and simulations at sufficient small propulsion speeds, we have observed qualitative and quantitative deviations that increase with the strength of the propulsion speed. We have discussed these deviations to be caused most probably by (i) the Kirkwood closure which we have applied in our theory, (ii) neglecting higher modes in an expansion of the pair-distribution function, and (iii) an assumption where we effectively neglect correlations beyond volume exclusion between a second particle and its surrounding ones. For this reason, future work should study how to improve closures and test the influence of higher modes. Note that improving on closures could also mean closing the Smoluchowski equation on an even higher level than we have done.

We have shown that our theory captures many effects that occur in systems of Brownian swimmers. Based on only the first two modes ζ_0 and ζ_1 in the expansion of the pair-distribution function, our analytic theory already successfully predicts the main directions of the conditional three-body forces, their linear dependence on the propulsion speed, and the effective swimming speed. These findings are in agreement with previous work. However, our approach does not yield independent expressions for ζ_0 and ζ_1. Such expressions would be necessary to obtain *a priori* theoretical predictions without further input of correlations. In any way, our theory has at least two levels of approximation. The first level is more general and is reached after closing our theory in Sec. II D and applying it to the special case of hard disks in Sec. II E. The second level is reached by applying the additional approximation from Eq. (30) in Sec. II F, which allows us to derive analytical expressions for the conditional three-body forces. We have shown that a numerical solution of our theory already on the first level is in very good agreement with our simulations such that the necessary parameters ζ_i in general could be obtained from numerical calculations.

In a next step, the parameters ζ_i could be used to predict physical quantities, for instance, phase separations like MIPS [9,23] and the pressure in active Brownian systems [25,26,71]. Another step could be the transfer of our findings to self-propelled Brownian swimmers in three dimensions. In conclusion, our detailed study of correlations in suspensions of active repulsive disks is a step towards an emerging liquid-state theory of scalar active matter.

ACKNOWLEDGMENTS

We acknowledge financial support from the German Research Foundation within the priority program SPP 1726 (Grant No. SP 1382/3-2) and through Grant No. INST 39/963-1 FUGG. We thank R. Wittkowski for helpful discussions. Further, we gratefully acknowledge computing time granted on the supercomputer Mogon at Johannes Gutenberg University Mainz and acknowledge support from the state of Baden-Württemberg through bwHPC.

APPENDIX: MODE EXPANSION

In Eq. (34) we expand the pair-distribution function $g(r,\theta)$ from Eq. (15) in Fourier modes. Accordingly, we find $\langle g(r,\theta)\rangle_\theta = g_0(r)$ and the projections of the conditional force $\vec{F}_1$ from Eq. (31) onto the directions $\hat{e}_r$ and $\hat{e}_\theta$ become

$$\hat{e}_r \cdot \vec{F}_1(r,\theta) = -\,\bar{\rho} \sum_{k=0}^{\infty} g_k(\sigma) A_k^{\mathrm{c}}(r)\cos(k\theta), \tag{A1}$$

$$\hat{e}_\theta \cdot \vec{F}_1(r,\theta) = -\,\bar{\rho} \sum_{k=0}^{\infty} g_k(\sigma) A_k^{\mathrm{s}}(r)\sin(k\theta). \tag{A2}$$

The mode-expansion coefficients A_k^{c} and A_k^{s} are defined using the r-dependent angle θ^* from Eq. (33) by

$$A_k^{\mathrm{c}}(r)\cos(k\theta) = \int_{\theta^*}^{2\pi-\theta^*} d\varphi\,\cos(\varphi)\cos[k(\varphi+\theta)], \tag{A3}$$

$$A_k^{\mathrm{s}}(r)\sin(k\theta) = \int_{\theta^*}^{2\pi-\theta^*} d\varphi\,\sin(\varphi)\cos[k(\varphi+\theta)]. \tag{A4}$$

The integrals in Eqs. (A3) and (A4) can be performed analytically and, for $k \in \{0,1\}$ and $1 \leqslant r \leqslant 2$, result in

$$A_0^{\mathrm{c}}(r) = -2\sin(\theta^*), \tag{A5}$$

$$A_1^{\mathrm{c}}(r) = [\pi - \theta^* - \sin(\theta^*)\cos(\theta^*)], \tag{A6}$$

$$A_0^{\mathrm{s}}(r) = 0, \tag{A7}$$

$$A_1^{\mathrm{s}}(r) = -[\pi - \theta^* + \sin(\theta^*)\cos(\theta^*)]. \tag{A8}$$

In general, for $r > 2$ all coefficients vanish except for $A_1^c = \pi$ and $A_1^s = -\pi$. At particle-particle contact with $r = 1$ the first coefficients are $A_0^c(\sigma) = -\sqrt{3}$, $A_1^c(\sigma) = \frac{2\pi}{3} - \frac{\sqrt{3}}{4}$, and $A_1^s(\sigma) = -\frac{2\pi}{3} - \frac{\sqrt{3}}{4}$.

When we insert the full expansion of the pair-distribution function $g(r,\theta)$ from Eq. (34) into the no-flux condition from Eq. (27) we achieve a set of equations, one for each occurring Fourier component $\cos(k\theta)$. Solving the equation for $k = 0$ with respect to $g_1(1)$, we obtain

$$g_1(1) = \frac{1}{K\bar{\rho}}\left(v_0 \pm \sqrt{v_0^2 + 8K\bar{\rho}J}\right), \tag{A9}$$

$$J = -\frac{\bar{\rho}}{4}\sum_{k=2}^{\infty} g_k(1)g_k(1)A_k^c + \sqrt{3}g_0(1)g_0(1)\bar{\rho} + g_0'(1), \tag{A10}$$

where $g_0'(1) = \frac{\partial}{\partial r}g_0(r)|_{r=1}$ and $K = (8\pi - 3\sqrt{3})/6 \approx 3.323$. In the limit of vanishing propulsion speed $v_0 \to 0$ all g_k for $k > 0$ must vanish. Accordingly, J must vanish and solely the plus sign in front of the square root in Eq. (A9) holds. A rearrangement of Eq. (A9) and using $\zeta_1 = \pi g_1(1)$ with $v_0 > 0$ leads to

$$v_0\left(1 - \bar{\rho}\frac{\zeta_1}{v_0}\frac{K}{\pi}\right) = \mp\sqrt{v_0^2 + 8K\bar{\rho}J}. \tag{A11}$$

The form of Eq. (A11) is interesting for the effective propulsion speed in the context of MIPS, as discussed by Bialké *et al.* [40] and by Stenhammar *et al.* (above Fig. 2 in their work) [69].

[1] N. P. Barry and M. S. Bretscher, Proc. Natl. Acad. Sci. USA **107**, 11376 (2010).
[2] S. Ramaswamy, Annu. Rev. Condens. Matter Phys. **1**, 323 (2010).
[3] V. Schaller, C. Weber, C. Semmrich, E. Frey, and A. R. Bausch, Nature (London) **467**, 73 (2010).
[4] C. Liu, X. Fu, L. Liu, X. Ren, C. K. Chau, S. Li, L. Xiang, H. Zeng, G. Chen, L.-H. Tang, P. Lenz, X. Cui, W. Huang, T. Hwa, and J.-D. Huang, Science **334**, 238 (2011).
[5] T. Sanchez, D. T. N. Chen, S. J. DeCamp, M. Heymann, and Z. Dogic, Nature (London) **491**, 431 (2012).
[6] J. Palacci, S. Sacanna, A. P. Steinberg, D. J. Pine, and P. M. Chaikin, Science **339**, 936 (2013).
[7] M. C. Marchetti, J. F. Joanny, S. Ramaswamy, T. B. Liverpool, J. Prost, M. Rao, and R. A. Simha, Rev. Mod. Phys. **85**, 1143 (2013).
[8] A. Bricard, J.-B. Caussin, N. Desreumaux, O. Dauchot, and D. Bartolo, Nature (London) **503**, 95 (2013).
[9] M. E. Cates and J. Tailleur, Annu. Rev. Condens. Matter Phys. **6**, 219 (2015).
[10] R. E. Goldstein, Annu. Rev. Fluid Mech. **47**, 343 (2015).
[11] W. Wang, W. Duan, S. Ahmed, A. Sen, and T. E. Mallouk, Acc. Chem. Res. **48**, 1938 (2015).
[12] J. Yan, M. Han, J. Zhang, C. Xu, E. Luijten, and S. Granick, Nat. Mater. **15**, 1095 (2016).
[13] R. Niu, T. Palberg, and T. Speck, Phys. Rev. Lett. **119**, 028001 (2017).
[14] A. Cavagna, A. Cimarelli, I. Giardina, G. Parisi, R. Santagati, F. Stefanini, and M. Viale, Proc. Natl. Acad. Sci. USA **107**, 11865 (2010).
[15] H. H. Wensink, J. Dunkel, S. Heidenreich, K. Drescher, R. E. Goldstein, H. Löwen, and J. M. Yeomans, Proc. Natl. Acad. Sci. USA **109**, 14308 (2012).
[16] J. R. Howse, R. A. L. Jones, A. J. Ryan, T. Gough, R. Vafabakhsh, and R. Golestanian, Phys. Rev. Lett. **99**, 048102 (2007).
[17] S. Gangwal, O. J. Cayre, M. Z. Bazant, and O. D. Velev, Phys. Rev. Lett. **100**, 058302 (2008).
[18] J. Palacci, C. Cottin-Bizonne, C. Ybert, and L. Bocquet, Phys. Rev. Lett. **105**, 088304 (2010).
[19] I. Theurkauff, C. Cottin-Bizonne, J. Palacci, C. Ybert, and L. Bocquet, Phys. Rev. Lett. **108**, 268303 (2012).
[20] I. Buttinoni, J. Bialké, F. Kümmel, H. Löwen, C. Bechinger, and T. Speck, Phys. Rev. Lett. **110**, 238301 (2013).
[21] M. Rubenstein, A. Cornejo, and R. Nagpal, Science **345**, 795 (2014).
[22] A. Wysocki, R. G. Winkler, and G. Gompper, Europhys. Lett. **105**, 48004 (2014).
[23] T. Speck, Eur. Phys. J. Spec. Top. **225**, 2287 (2016).
[24] B. van der Meer, L. Filion, and M. Dijkstra, Soft Matter **12**, 3406 (2016).
[25] A. P. Solon, J. Stenhammar, R. Wittkowski, M. Kardar, Y. Kafri, M. E. Cates, and J. Tailleur, Phys. Rev. Lett. **114**, 198301 (2015).
[26] T. Speck and R. L. Jack, Phys. Rev. E **93**, 062605 (2016).
[27] A. Farutin, S. Rafaï, D. K. Dysthe, A. Duperray, P. Peyla, and C. Misbah, Phys. Rev. Lett. **111**, 228102 (2013).
[28] J. Toner and Y. Tu, Phys. Rev. E **58**, 4828 (1998).
[29] J. L. Anderson, Annu. Rev. Fluid Mech. **21**, 61 (1989).
[30] M. Reichert and H. Stark, Eur. Phys. J. E **17**, 493 (2005).
[31] Y. Yang, F. Qiu, and G. Gompper, Phys. Rev. E **89**, 012720 (2014).
[32] D. Marenduzzo, E. Orlandini, M. E. Cates, and J. M. Yeomans, Phys. Rev. E **76**, 031921 (2007).
[33] M. E. Cates, S. M. Fielding, D. Marenduzzo, E. Orlandini, and J. M. Yeomans, Phys. Rev. Lett. **101**, 068102 (2008).
[34] T. Vicsek, A. Czirók, E. Ben-Jacob, I. Cohen, and O. Shochet, Phys. Rev. Lett. **75**, 1226 (1995).
[35] A. Czirók and T. Vicsek, Physica A **281**, 17 (2000).
[36] J. Tailleur and M. E. Cates, Phys. Rev. Lett. **100**, 218103 (2008).
[37] R. W. Nash, R. Adhikari, J. Tailleur, and M. E. Cates, Phys. Rev. Lett. **104**, 258101 (2010).

[38] M. E. Cates, Rep. Prog. Phys. **75**, 042601 (2012).
[39] M. E. Cates and J. Tailleur, Europhys. Lett. **101**, 20010 (2013).
[40] J. Bialké, H. Löwen, and T. Speck, Europhys. Lett. **103**, 30008 (2013).
[41] S. K. Das, S. A. Egorov, B. Trefz, P. Virnau, and K. Binder, Phys. Rev. Lett. **112**, 198301 (2014).
[42] K. H. Nagai, Y. Sumino, R. Montagne, I. S. Aranson, and H. Chaté, Phys. Rev. Lett. **114**, 168001 (2015).
[43] R. Ni, M. A. C. Stuart, and P. G. Bolhuis, Phys. Rev. Lett. **114**, 018302 (2015).
[44] A. Wysocki, J. Elgeti, and G. Gompper, Phys. Rev. E **91**, 050302 (2015).
[45] A. M. Menzel, A. Saha, C. Hoell, and H. Löwen, J. Chem. Phys. **144**, 024115 (2016).
[46] A. Tiribocchi, R. Wittkowski, D. Marenduzzo, and M. E. Cates, Phys. Rev. Lett. **115**, 188302 (2015).
[47] R. Wittkowski, J. Stenhammar, and M. E. Cates, New J. Phys. **19**, 105003 (2017).
[48] T. Speck, J. Bialké, A. M. Menzel, and H. Löwen, Phys. Rev. Lett. **112**, 218304 (2014).
[49] J.-P. Hansen and I. R. McDonald, *Theory of Simple Liquids*, 4th ed. (Elsevier, Amsterdam, 2013).
[50] T. Speck, A. M. Menzel, J. Bialké, and H. Löwen, J. Chem. Phys. **142**, 224109 (2015).
[51] K. Zahn, G. Maret, C. Ruß, and H. H. von Grünberg, Phys. Rev. Lett. **91**, 115502 (2003).
[52] J. Bartnick, M. Heinen, A. V. Ivlev, and H. Löwen, J. Phys.: Condens. Matter **28**, 025102 (2016).
[53] J. G. Kirkwood, J. Chem. Phys. **3**, 300 (1935).
[54] J. de Boer and A. Michels, Physica **6**, 97 (1939).
[55] F. H. Stillinger, J. Chem. Phys. **57**, 1780 (1972).
[56] J. Fischer, Mol. Phys. **33**, 75 (1977).
[57] L. L. Lee, J. Chem. Phys. **135**, 204706 (2011).
[58] N. G. V. Kampen, Physica **27**, 783 (1961).
[59] J. A. Barker and D. Henderson, Rev. Mod. Phys. **48**, 587 (1976).
[60] A. Einstein, Ann. Phys. (Leipzig) **19**, 371 (1906).
[61] D. Richard, H. Löwen, and T. Speck, Soft Matter **12**, 5257 (2016).
[62] H. C. Andersen, J. D. Weeks, and D. Chandler, Phys. Rev. A **4**, 1597 (1971).
[63] P. Attard, Mol. Phys. **74**, 547 (1991).
[64] J. Bialké, T. Speck, and H. Löwen, J. Non-Cryst. Solids **407**, 367 (2015).
[65] J. A. Barker and D. Henderson, J. Chem. Phys. **47**, 4714 (1967).
[66] W. H. Press, S. A. Teukolsky, W. T. Vetterling, and B. P. Flannery, *Numerical Recipes in C*, 2nd ed. (Cambridge University Press, Cambridge, 1992).
[67] T. Hanke, C. A. Weber, and E. Frey, Phys. Rev. E **88**, 052309 (2013).
[68] Y.-L. Chou and T. Ihle, Phys. Rev. E **91**, 022103 (2015).
[69] J. Stenhammar, A. Tiribocchi, R. J. Allen, D. Marenduzzo, and M. E. Cates, Phys. Rev. Lett. **111**, 145702 (2013).
[70] T. F. F. Farage, P. Krinninger, and J. M. Brader, Phys. Rev. E **91**, 042310 (2015).
[71] J. Bialké, J. T. Siebert, H. Löwen, and T. Speck, Phys. Rev. Lett. **115**, 098301 (2015).